UNIVERSITY OF GRONINGEN

FACULTY OF SCIENCE AND ENGINEERING

MASTER THESIS

Ion Guiding and Ion Extraction from the CISe Gas Catcher

Author:
L. VAN DER WERFF

First supervisor:
Prof. Dr. J. EVEN
Second supervisor:
Dr. C.E. RIGOLLET

August 30, 2022

Abstract

Gas catchers are widely used for stopping and thermalizing high-energetic nuclear reaction products to perform high precision mass measurements. The general idea of a gas catcher is to reduce the level of impurities in the buffer gas to increase the extraction efficiency. However, the Chemical Isobaric Separation (CISe) technique for the separation of isobars aims to make use of the chemistry inside the gas catcher. The goal of this research project is to study the ion guiding and ion extraction from the gas catcher in off-line measurements. An electrode system, consisting of RF- and DC electric fields, is used to guide and extract the ions. A low-energy radioactive ion source, ^{223}Ra, was mounted inside the gas catcher to produce ions. A silicon detector was installed behind the gas catcher to identify the extracted ions by measuring the energies of their emitted α-particles. Based on the measurements, it was concluded that ^{211}Bi ions were extracted from the gas catcher, but not the short-lived ^{219}Rn ions. From the studies, it is proposed how to improve the ion guiding process.

Dankwoord

Het afstudeerproject was lang een groot obstakel op mijn pad. Na veel en lang nadenken, besloot ik om door te gaan. Een verandering van onderwerp naar experimenteel onderzoek heeft mij geholpen en langzaam begon ik plezier te krijgen in het werk dat ik deed. Ik ben trots dat ik dit avontuur heb weten door te zetten. Wat moeilijk begon, is goed geëindigd. Een hele grote groep mensen heeft mij door dit jaar heen gesleept en ik wil hen graag bedanken.

Allereerst wil ik mijn supervisor Julia Even bedanken voor haar enthousiasme en hulp die ze mij ook dit jaar heeft gegeven. Ik ben blij dat ik mijn beide afstudeerprojecten bij haar kon doen. Ze was begripvol en stond altijd voor mij klaar om vragen te beantwoorden, peptalks te geven en om mij op te vrolijken met chocola, taart, ijsjes en bloedsinaasappels. Naast de serieuze momenten was er ook ruimte voor de niet-serieuze momenten tussen het werken door. Het fietsen in extreme weersomstandigheden, nieuwe woorden bedenken en "het diner" vallen onder de hoogtepunten.

Als tweede wil ik graag mijn andere supervisor Catherine Rigollet bedanken voor het ondersteunen van mijn project. Ze moedigde me aan wanneer dit nodig was en was altijd bereid om mij te helpen. Daarnaast wil ik ook graag haar zoon, Leo, bedanken voor het schrijven van een programmaatje dat hielp om data in het goede formaat te krijgen om te verwerken.

Ik wil graag Nathan Moorrees bedanken voor het altijd klaar staan om problemen op te lossen. Als er iets niet werkte, kon ik altijd bij jou terecht om samen te zoeken naar de oplossing. Soms ging dat heel snel en soms duurde het wat langer. Ook waardeer ik de leuke en interessante gesprekken die we hebben gevoerd.

Mijn andere collega's en ex-collega's van de onderzoeksgroep wil ik ook graag bedanken voor de leuke momenten die we hebben beleefd: Arif, Xiangcheng, Lennart, Leo en Ludovica. Jullie maakten het project draaglijker en ik ben blij dat ik onderdeel mocht zijn van deze groep.

Ik wil graag Mark van de elektronische workshop bedanken voor zijn hulp met de RF carpet. Met problemen kon ik altijd bij hem terecht, ook al was het de zoveelste keer. Ik hoop dat er een dag komt dat alle problemen met de RF carpet zijn opgelost.

Daarnaast wil ik graag Leo Huisman bedanken. Hij was altijd behulpzaam met vragen over verschillende benodigdheden.

Een heel speciaal bedankje gaat uit naar mijn wandelvrienden van de workshop: Dirk, Floris, Henk, Martin en Michel. Niet alleen waren jullie altijd in een mum van tijd klaar om benodigde onderdelen te maken, jullie namen mij ook op in jullie groep. De vele middagwandelingen, de koffie (chocolademelk) breaks en de gesprekken maakten het werk een stuk leuker en gezelliger. Ik vind jullie werk zeer interessant en ik kijk met volle bewondering hoe jullie producten uitwerken en maken. Het afgelopen jaar heb ik veel van jullie geleerd. Bedankt voor alle leuke momenten.

Daarnaast wil ik graag mijn lieve vrienden bedanken voor hun mental support en de nodige afleiding. Ik wil specifiek Gijsbert bedanken voor het samen sporten en pizza eten, wat heeft geholpen om te ontspannen. De gesprekken die we hebben gevoerd waren altijd fijn en behulpzaam. Bedankt voor alle steun die je mij hebt gegeven.

Als laatste wil ik graag mijn ouders bedanken. Ook zij gingen mee in alle ups en downs die dit jaar met zich meebracht. Zonder hun steun was dit jaar een stuk moeilijker geweest. Mama die extra bakjes eten voor mij maakte en de wekelijkse wandelingen met papa hebben mij veel geholpen. Ze waren altijd enthousiast over mijn project en lieten het niet blijken wanneer ik weer eens abracadabra tegen ze sprak. Bedankt voor jullie interesse.

Contents

1 Introduction

1.1 Motivation

High precision mass measurements of exotic nuclei are of great interest for nuclear structure and nuclear astrophysics. From these measurements the nuclear binding energies can be determined, and thus we can pin down the location of nuclear shells. The magic numbers corresponding to the nuclear shell closures are indicated in Figure 1 by the horizontal and vertical black lines. Nuclei with a filled proton shell or a filled neutron shell are called magic nuclei. When both nuclear shells of the protons and neutrons are filled, they are called doubly-magic nuclei. The aim of our research is to access the neutron-deficient region around the doubly-magic ^{100}Sn which is indicated in Figure 1. Nuclei in this region can, for example, be produced in fusion-evaporation reactions. The main challenges arise from low production yields, short half-lives, and unwanted by-products.
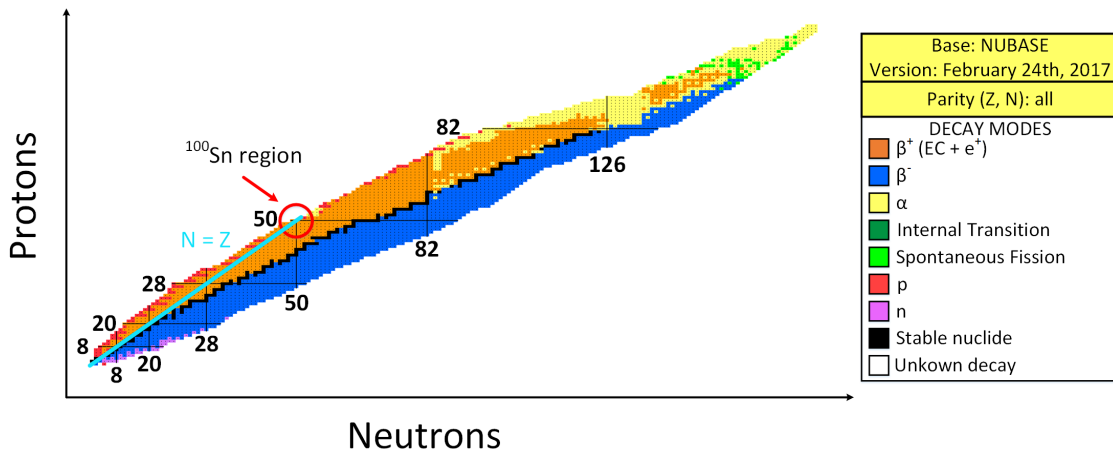

Figure 1: *Nuclear chart [1]. The region of interest is indicated in the figure by the red circle. The decay modes of the nuclei are indicated by the color code. Black squares correspond to the valley of stability. The horizontal and vertical black lines indicate the shell closures, known as the magic nuclei. The light blue arrow indicates the nuclei with an equal number of neutrons and protons, the N = Z nuclei.*

Doubly-magic ^{100}Sn is of particular interest because it is one of the heaviest nuclei with the same number of neutrons and protons, $N = Z = 50$. It is also relevant to the rapid-proton (rp) capture, as it lies at the end of the rp-process. Improving the understanding of the rp-process, results in a better interpretation of X-ray bursts [2]. The rp-process consists of rapid proton-capture reactions to produce heavier proton-rich elements and subsequent slow β^+-decay. Figure 2 shows a close-up of the mass accuracy of the ^{100}Sn region of the nuclear chart [1]. The predicted path of the rp-process is indicated in Figure 2 with the white lines [2], and the $N = Z$ nuclei are indicated with the yellow line.

The atomic masses in the region of ^{100}Sn are not known with high precision yet, which is crucial to better understand the path of the rp-process. Mass measurements in the vicinity of ^{100}Sn have already been performed and give more insights in the understanding of ^{100}Sn [3, 4]. For measurements in the ^{100}Sn region, the main challenge is, besides low production rates, the separation of isobaric contaminants. These are nuclides with the same mass number as the ion of interest. In 1996, the mass of ^{100}Sn has been measured using the cyclotron in GANIL, where ^{100}Sn is produced in fusion-evaporation reactions between a ^{50}Cr beam and a ^{58}Ni target [5]. The masses of ^{100}Sn, ^{100}In, and ^{100}Cd were measured by using ^{100}Ag as a reference. The mass of ^{100}Sn was measured with a precision of 10^{-5}, which was limited by low statistics [5].

The mass precision can be improved by using a Penning trap mass spectrometer, such as SHIP-TRAP [6]. The Penning trap technique is very precise and does not require a large number of

detected ions. The main challenge in the measurements using the Penning trap technique is the slowing down of the incoming high energetic beam and the mass separation from its isobars. SHIP is not designed to separate isobaric nuclides. An additional separation step using a new gas catcher is introduced. Gas catchers are used for stopping and thermalizing the high-energetic nuclear reactions products [7–9]. The general idea of a gas catcher is to reduce the level of impurities in the buffer gas to prevent ion losses. However, a novel technique for the separation of isobars is under development, which aims to make use of the chemistry inside the gas catcher operated at room temperature. This is called the Chemical Isobaric Separation (CISe) technique.
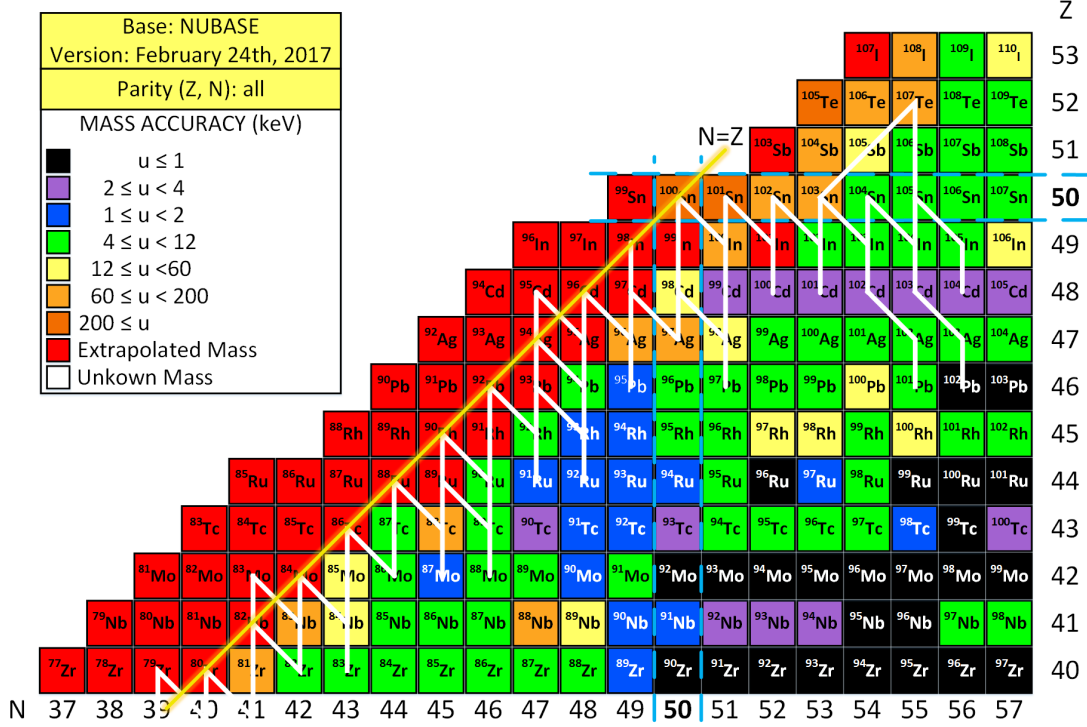

Figure 2: *Close-up of the ^{100}Sn region of the nuclear chart. The mass accuracy of the nuclei is indicated by the color code [1]. The predicted rp-path is indicated by the white lines [2]. The yellow line indicates the N = Z nuclei. The dashed blue lines indicate ^{100}Sn, the nucleus with an equal number of protons and neutrons.*

1.2 CISe project

The Chemical Isobaric Separation (CISe) project aims to access the neutron-deficient isotopes in the ^{100}Sn region [10]. This will be realized by taking advantage of the gas-phase chemistry inside the gas catcher for the separation of isobars by adding a combination of the helium buffer gas and a reactive gas. This makes it possible to separate ^{100}Sn from ^{100}In, ^{100}Cd, and ^{100}Ag due to the different chemical properties. One potential method to separate ^{100}Ag and ^{100}Cd from ^{100}Sn and ^{100}In, is by adding CH_4 as a reactive gas. Cd^+ and Ag^+ react with methane and form clusters in the following way [11]:

$$Cd^+ + CH_4 \rightarrow Cd^+(CH_4) \tag{1}$$

$$Ag^+ + CH_4 \rightarrow Ag^+(CH_4) \tag{2}$$

The Sn^+ and In^+ ions do not react with methane [11]. This technique can be used to test the chemical separation of the stable isotopes in an offline setup. Later, the chemistry inside the gas catcher can be implemented in on-line experiments for the study of exotic nuclei.

As shown in Figure 3, the CISe setup consists of a gas catcher that is connected to a quadrupole Time-of-Flight (qToF) via an ion guide consisting of two hexapoles. The ions are created by laser ablation in the gas catcher, where 50 mbar of helium and a reactive gas are added. The ions slow down by colliding with the helium buffer gas and might react with the reactive gas. The aim is to find a reactive gas that reacts with the ion of interest and not with its isobaric contaminants, or vice versa. Then, the different ions are extracted from the gas catcher to the ion guide. Simulations of the ion trajectories of atomic- (e.g. Ag^+) and molecular ions ($AgCH_4^+$) through the ion guide system have been performed by A. Mollaebrahimi [12], and show an overall transmission efficiency above 90% for both atomic- and molecular ions. From the ion guide, the ions are transported to the quadrupole Time-of-Flight (qToF). The ions are either detected at the dynolite-point detector or at the Micro-Channel Plate (MCP) detector. The MCP detector registers the time-of-flight to determine the mass-to-charge ratio (m/q) of the ions.

The CISe setup will be used to find the optimal chemical system for the separation of ^{100}Sn from its isobars by studying different reactive gases (e.g. CH_4, H_2O, etc.). Once the optimum operating conditions are found, the gas catcher will be implemented at SHIP for on-line experiments.
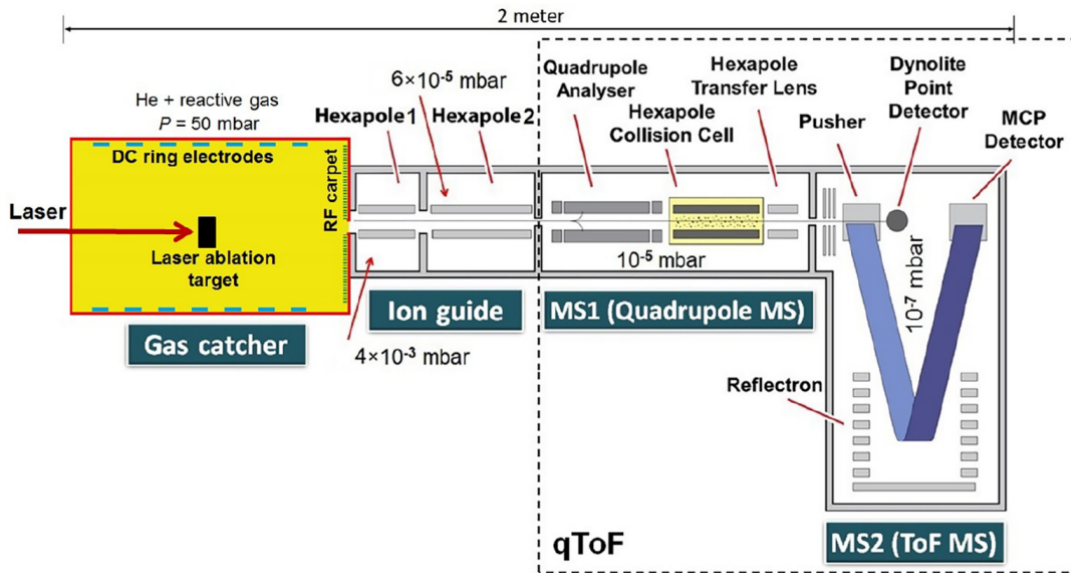

Figure 3: *Schematic diagram of the CISe setup, where a gas catcher is coupled to a commercial qToF via an ion guide consisting of two hexapoles. The qToF is a Quadrupole Mass Spectrometer (Quadrupole MS) coupled with a reflection Time-of-Flight Mass Spectrometer (ToF MS). Figure adapted from Ref. [10].*

1.3   Aim of this research

Before the chemical reactions in the gas catcher can be studied, it is necessary to optimize the ion guiding and extraction from the gas catcher in off-line measurements. This is realized by designing a detector holder, which was installed behind the RF carpet (Figure 3). Instead of using the laser ablation source, a low-energy radioactive ion source, ^{223}Ra, was mounted inside the gas catcher. This radioactive ion source was chosen to perform extraction studies independent of the laser ablation source. The ions are slowed down by collisions with the helium buffer gas, and are guided by DC electric fields and the RF carpet to the exit hole. At this orifice, the gas flow takes over and extracts the ions from the gas catcher. The silicon detector, which was installed behind the carpet, identifies the extracted ions by measuring the energies of their emitted α-particles. The obtained characteristic α-spectrum can be used to determine the extraction efficiency from the gas cell. This research supports later experiments performed with the CISe setup [10].

2 Methods and techniques

As described in Section 1.3, the focus of this research is on the extraction of ions from the gas catcher (Figure 3). This chapter explains the methods used to guide, extract, and detect these ions. Section 2.1 focuses on the physical processes in- and the ion extraction from the gas catcher. Behind the gas cell, a silicon surface barrier detector is installed. More details about α-spectrometry, the silicon detector, and radioactive sources are given in Section 2.2.

2.1 Physical processes in the gas catcher

Gas catchers are widely used to slow down high-energetic nuclear reaction products through interactions with a buffer gas [13,14]. The incoming ions have energies in the order of a few MeV and are slowed down to energies of a few eV by ionizing the buffer gas atoms. In this process, highly-charged ions reduce to singly or doubly charged ions. The thermalized ions are transported and extracted via electric fields and the gas flow. Gas catchers can be operated at cryogenic- [9,15] or room temperature [16,17]. Physical processes play a role in guiding and extracting these ions from the gas catcher, which will be described in this section.

Ions lose energy by ionization and excitation of atoms. They collide with the buffer gas atoms, e.g. argon or helium, which has a strong effect on the ion survival probability and the extraction efficiency in the gas cell. The higher the buffer gas pressure in the gas cell, the higher the collision probability of the ion. The helium gas density is lower than the argon gas density [18]. Thus, ions have a larger range in the helium gas. Another advantage of using helium as a buffer gas is the large first ionization potential of helium (24.6 eV). Because of this, thermalized ions cannot neutralize in the collisions: the nuclear recoils remain singly or doubly charged. However, there might still be losses due to impurities in the gas [13]. Impurities can lead to formation of molecules and charge-exchange reactions. Molecular formation leads to a change in the ion mobility. An ion of interest X^+ reacts with a ligand molecule M originating from impurities in the helium buffer gas:

$$X^+ + M \rightarrow X^+M^* \tag{3}$$

Through collisions with the helium buffer gas, the X^+M^* molecule can be stabilized:

$$X^+M^* + He \rightarrow XM^+ + He^* \tag{4}$$

A technique to reduce the impurities in the gas is by freezing them out [9]. For gas catchers operated at room temperature, ultra-high vacuum (UHV) conditions and ultra-pure helium, at sub-ppb impurity concentrations, are required [14,16].

During the stopping process of the incoming ions, a large amount of ion-electron pairs are created due to the ionization of the buffer gas atoms [19]. Under the influence of the applied DC field, the ions and electrons move in opposite directions. Since the mass of electrons is much smaller compared to the ions, their mobility is much larger, resulting in a lower electron density. While the electrons are removed, the positively charged ions stay behind, which will lead to space-charge effects [20–22]. Recombination of thermalized ions occurs when electrons and ions are not pulled apart fast enough due to a large ionization degree. This creates a plasma which shields the applied electric field and leads to free electrons available for recombination [23,24]:

$$X^+ + e^- + He \rightarrow X + He \tag{5}$$

where X is the ion of interest, e^- is the electron, and He is the helium buffer gas atom. To reduce the probability of recombination, a high electric field gradient for the separation of electrons and ions is required. This will also result in a shorter extraction time.

After thermalization, the ions are guided by electric fields for fast and efficient extraction. The maximum electric field that can be applied depends on the breakdown voltage, also known as

Paschen's law [25]. During the ion transport, diffusion losses might occur. The diffusion time can be calculated with the following equation [26]:

$$\tau_D = \frac{1}{D} \left(\frac{r_0}{2.405} \right)^2 \qquad (6)$$

where τ_D is the diffusion time, D is the diffusion coefficient, and r_0 is the radius of the gas catcher. The diffusion coefficient is calculated using equations [27]:

$$D = \frac{k_B T K}{q} \qquad (7) \qquad\qquad K = K_0 \frac{T}{T_0} \frac{p_0}{p} \qquad (8)$$

where k_B is the Boltzmann constant, T is the temperature, q is the ion charge, K is the ion mobility, p is the pressure, T_0 is the standard temperature (273.15 K), p_0 is the standard pressure (1013 mbar), and K_0 is the reduced ion mobility which can be found in literature for most elements. When the gas catcher is operated at a pressure of 50 mbar at room temperature, $K_0 = 17.37$ V/cm for ^{219}Rn, and the radius of the gas catcher is $r_0 = 14$ cm, the diffusion time is calculated to be $\tau_D = 3.4$ s [27]. This is long compared to typical extraction times from gas catchers operated at a pressure of ~ 50 mbar at room temperature, which are on the order of a few tens of ms [28]. Thus, diffusion losses are of minor importance during ion transport.

In this study, the gas catcher is operated at room temperature, which means the impurity level is of great importance. A DC electric field is needed for fast ion extraction, but also to prevent neutralization due to recombination.

2.1.1 Ion extraction from the gas catcher

There are several methods to extract the ions from the gas catcher. One of the methods is using only a gas flow, which is created by the pressure difference between the gas cell and the ion guide [29]. This extraction method is rather slow and might not be fast enough to avoid ion neutralization. Another method is to extract the ions using a combination of a gas flow and DC fields [30]. A third method is a combination of the gas flow and a RF carpet or RF funnel, guiding the ions with electric fields [7–9, 16, 26]. The working principle of both the RF carpet and the RF funnel is the same: an RF voltage is applied to concentric ring electrodes, which decrease in diameter towards an extraction orifice. The advantage of a RF carpet is the printed circuit board (PCB) technology, which has a finer electrode structure compared to the RF funnel. This leads to an increase in the maximum RF repelling force from the carpet on the ions. However, the fine electrode structure is also sensitive to discharges. The breakdown voltage is given by the Paschen curve [25], which is dependent on the pressure and the applied voltage. Another disadvantage might be the evaporation of impurities from the PCB material when operating the system at room temperature. In this study, a combination of the gas flow and a RF carpet is used to extract the ions.

Working principle of the RF carpet

The main function of the carpet is to transport and focus the ions towards the extraction orifice. This is realized by using a RF field and a DC gradient. An illustration of the working principle of the carpet is shown in Figure 4, where DC_{cage} represents the electric field of the cage, pushing the ions towards the carpet. The RF voltage supplies an alternating repelling force (F_{RF}) with a 180° phase difference between adjacent electrodes, which makes the ions hover in front of the carpet. In addition to the RF voltage, a traveling potential wave with a 90° phase difference is superimposed to the electrodes to create a DC gradient. The combination of the RF- and DC fields result in ions "surfing" over the surface of the carpet towards the exit hole [31–33]. At the exit hole, the ions are extracted by a supersonic gas-jet due to the pressure difference between the gas catcher and the ion guide. The ion transportation time is determined by the wave voltage and speed. Small wave amplitudes result in ions slipping out of the traveling potential wave: the ion velocity is smaller than the wave velocity ($v_i < v_w$). At certain increased wave amplitudes, the ions are carried by the traveling potential wave: the ions move with a velocity equal to the wave velocity ($v_i = v_w$). To optimize the ion extraction, the values given to the RF- and DC fields need to be tuned.
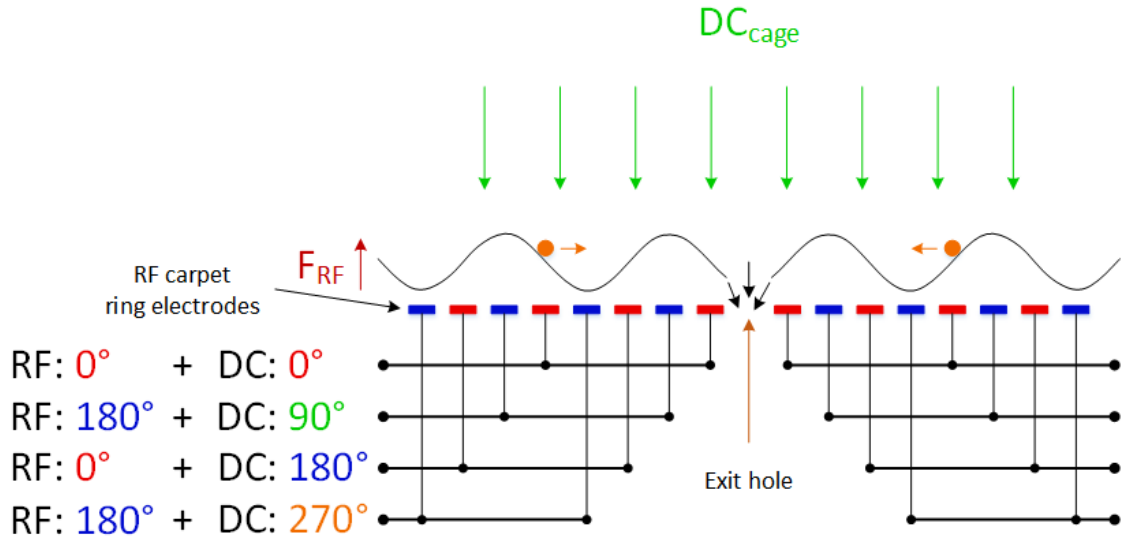
7

Figure 4: *Concept of the ion surfing method of the RF carpet, showing the RF- and DC fields. The DC_{cage} (green arrows) represents the electric field gradient of the cage, pushing the ions towards the carpet. F_{RF} (red arrow) represents the time-average repelling force due to the RF voltage, which make the ions hover in front of the carpet. The applied $90°$ phase difference to produce a traveling potential wave is indicated in the figure. Due to the RF- and DC fields of the carpet, the ions (orange circles) "surf" over the carpet as a traveling wave towards the exit hole (black arrows). Figure adapted and modified from Ref. [33].*

2.2 α-spectrometry

To determine if the ions are guided and extracted from the gas catcher to the ion guide, as shown in Figure 3, α-spectrometry measurements are performed. α-spectrometry is used to identify the extracted radionuclides based on their α-particles emitted in the decay process. The α-decay is characterized as:

$$^{A}_{Z}\text{X} \rightarrow ^{A-4}_{Z-2}\text{Y} + ^{4}_{2}\text{He}$$
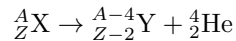
The α-particles are mono-energetic, which means they are emitted with a characteristic energy. This makes it easy to identify the decaying radionuclides. Using an α-source as a probe, to study the ion transport and the ion extraction efficiency from the gas catcher, is a well-known employed method [8,9,15,17,34–37]. The setup for the α-spectrometry measurements is explained in chapter 3.

A detector is needed to measure the emitted α-particles. There are two types of silicon detectors used for α-spectrometry: Passivated Implanted Planar Silicon (PIPS) detectors and Silicon Surface Barrier (SSB) detectors. In the experiments performed in this research, a silicon surface barrier detector is used. The working principle is explained in Section 2.2.1. Section 2.2.2 contains more details about the radioactive sources that were used in this work.

2.2.1 Silicon Surface Barrier detector

A silicon semiconductor detector is installed behind the carpet to detect the radioactive ions that are extracted from the gas cell. Silicon detectors are reverse biased and consist of a combination of p-type and n-type silicon materials, which are created by adding an impurity to the pure silicon material [38]. The reverse bias is created by applying a positive voltage to the n-type silicon. P-type silicon contains a small amount of acceptor impurities: it has an excess of holes in the valence band, whereas n-type silicon contains a small amount of donor impurities: it contains more electrons than holes in the conduction band [39]. Hence, adding impurity atoms to the silicon

result in the characteristic charge carriers of the semiconductor. Combining the p-type and n-type silicon results in a p-n junction. This leads to a depletion region, which is free of electrons and holes. Emitted α-particles entering the silicon detector lose a small amount of energy and create electron-hole pairs. The average energy needed to create an electron-hole pair in silicon is $3.62\,\mathrm{eV}$ at room temperature [39]. The electron-hole pairs result in an electrical signal proportional to the energy of the α-particle. The measured α-energies identify the radioactive isotopes. The resulting α-spectrum is specific for the mother isotope.

The energy resolution is dependent on the electronic noise from the leakage current, capacitance, and the bias resistor, as well as the energy loss and straggling in the detector's entrance window. The leakage current is strongly dependent on the type and temperature of the detector. Higher leakage currents result in larger electronic noise, which is why low leakage currents are desirable. The electronic noise of the leakage current and capacitance will be minimized using the optimal settings for the shaping-time constant of the amplifier. The noise of the bias resistor is usually negligible, but for high detector temperatures, it might be necessary to decrease the value of the bias resistor. This results in a higher electronic noise. The energy loss and straggling in the entrance window of the detector is dependent on the angle at which the α-particles enter. If they enter perpendicular to the detector, the resulting energy loss is minimal. However, if they enter at an angle, they have to pass through a thicker layer of material, which results in a higher energy loss, thus, a lower energy resolution. Many more parameters have an effect on the performance of the detector [40]. In general, the resolution is better for smaller detectors, but the counting efficiency is better for larger detectors. Hence, depending on what is needed, a compromise has to be made to find the optimal working settings of the detector.

2.2.2 Radioactive sources

In this research, two different radioactive sources were employed: an ^{241}Am alpha source and a ^{223}Ra ion source. The ^{241}Am was used to become acquainted with α-spectrometry and to perform detector tests. The α-spectrum is well-known, showing two distinct ^{241}Am peaks. The decay properties of ^{241}Am are given in Table 1, Section 2.2.3.

The ^{223}Ra ion source also has a well-known, easily identifiable α-spectrum. However, it contains a long-lived parent and a number of short-lived daughter nuclei in transient equilibrium, which makes the spectrum a little more complex compared to the spectrum from ^{241}Am. Its decay properties are given in Table 2, Section 2.2.4. ^{223}Ra is chosen as an ion source due to the short half-life of its daughter nucleus, ^{219}Rn ($t_{1/2} = 3.96\,\mathrm{s}$). It is quick and easy to determine whether the ions have been extracted. Another advantage is the relatively short half-life of the parent nucleus, ^{223}Ra ($t_{1/2} = 11.44\,\mathrm{d}$). If there is a contamination on the detector, it takes a couple of months for the ^{223}Ra to decay, which is relatively fast.

The ^{223}Ra ion source is prepared from an open ^{227}Ac source, its decay chain is shown in Figure 5. ^{227}Ac has a very long half-life ($t_{1/2} = 21.77\,\mathrm{y}$), which makes it easy to prepare fresh ^{223}Ra ion sources. The preparation is done in our own laboratory at the University of Groningen. Only a very thin layer of radioactive material is deposited on the source screw. If the source is too thick, the energy resolution decreases, and small detailed peaks are not well resolved. More information about the source preparation can be found in Section 4.2.1 from Ref. [41].

One physical effect that has to be considered is the loss of the ^{219}Rn isotopes. The ^{219}Rn isotopes can be used to study the ion transport. Radon is a noble gas, which is transported in a gas stream. The radon has to be filtered from the gas stream and captured in front of the detector. This is done by installing an ion catcher foil in front of the detector. The catcher foil captures the ^{219}Rn nuclei, from which they decay to the detector.

The absolute activity of the ion source can be calculated using the following equation:

$$A = A_M \frac{\text{Surface area detector}}{\text{Area detector}}$$
$$= \frac{\Sigma_\alpha}{t_L} \frac{4\pi s^2}{\pi r^2} \tag{9}$$

where A_m is the measured activity of the sum of all the detected peaks divided by the live time, t_L, s is the distance between the source and the detector, and r is the radius of the active area of the detector.

2.2.3 Decay properties ^{241}Am

^{241}Am decays to excited ^{237}Np states via α-decay. The α-decay energies with their respective branching ratios are given in Table 1. The branching ratio means that in 100 decays, $\sim 84\,\alpha$-particles with an energy of 5485.56 keV and 13 α-particles with an energy of 5442.80 keV are emitted. The remaining 3 % are distributed over the other decay channels. Hence, two clearly distinguishable peaks are expected to be found in the measurements (Am I/Am II).

Table 1: *Decay properties of ^{241}Am. The data are taken from [42].*

Isotope	Half life	Decay mode	Notation used	Energy (keV)	Branching ratio (%)
^{241}Am	432.2 y	α		5388.23(13)	1.6(2)
		α	Am II	5442.80(13)	13.0(6)
		α	Am I	5485.56(12)	84.5(10)
		α		5511.47(13)	0.22(3)
		α		5544.5(16)	0.34(5)

2.2.4 Decay properties ^{223}Ra

The decay chain of ^{223}Ra is shown in Figure 5, and the decay properties are given in Table 2. It is expected to measure eight different peaks when the source is in front of the detector (Figure 7), depending on the energy resolution of the detector: two of ^{223}Ra (Ra I/Ra II), three of ^{219}Rn (Rn I/Rn II/Rn II), one of ^{215}Po (Po), and two of ^{211}Bi (Bi I/Bi II).
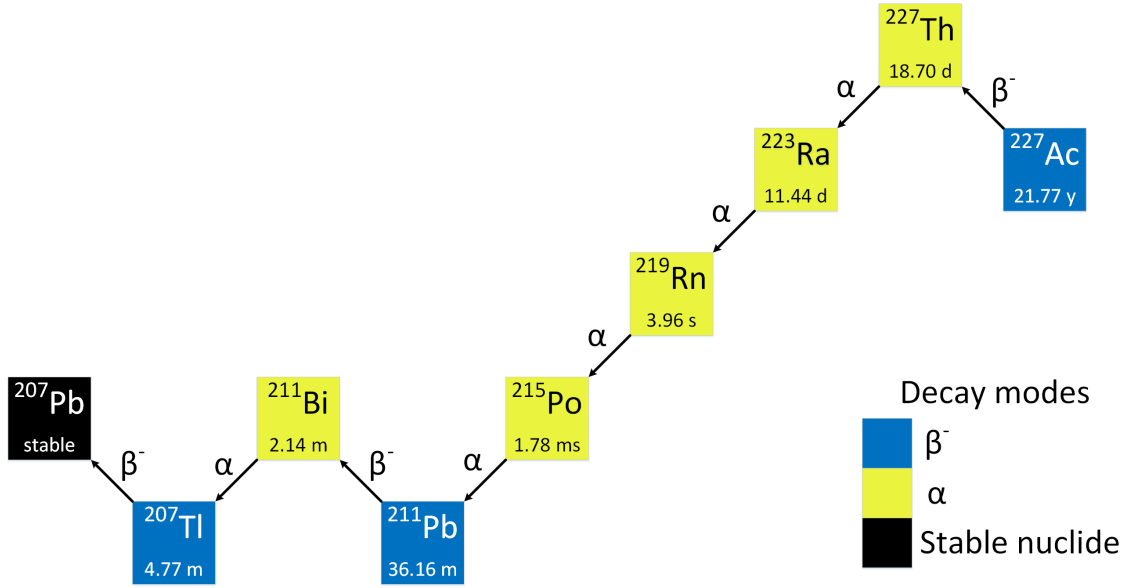
Figure 5: *Decay chain of* ^{227}*Ac. The half-lives of each nuclide are indicated below the isotope symbols. The source installed in the vacuum chamber is* ^{223}*Ra. The blue boxes indicate* β^-*-decaying isotopes, the yellow boxes indicate* α*-decay, and the black box indicates a stable nuclide.*

Table 2: *Decay properties of* ^{223}*Ra. The data are taken from [43].*

Isotope	Half life	Decay mode	Notation used	Energy (keV)	Branching ratio (%)
^{223}Ra	11.44 d	α		5539.80(90)	9.2(2)
		α	Ra II	5606.73(30)	25.7(5)
		α	Ra I	5716.23(29)	52.6(13)
		α		5747.0(4)	9.2(2)
^{219}Rn	3.96 s	α	Rn III	6426.0(10)	7.5(6)
		α	Rn II	6552.6(10)	12.9(6)
		α	Rn I	6819.1(3)	79.4(10)
^{215}Po	1.78 ms	α	Po	7386.2(8)	100
^{211}Pb	36.1 min	β^-		1372 (endpoint)	100
^{211}Bi	2.14 min	α	Bi II	6278.2(7)	16.23(14)
		α	Bi I	6622.9(6)	83.77(14)

3   Experimental setup

Two different setups were used in this work: a test setup was built to test the silicon detectors, and, subsequently, the silicon detector was mounted inside the CISe setup behind the carpet. This chapter gives an overview of both setups, and describes the equipment used.

3.1   Test setup

A box of old silicon detectors was made available for this project. The first step was to determine which ones were working, and to get familiar with the equipment. This required to build the test setup.

A silicon detector was placed inside a vacuum chamber, which was connected to a vacuum pump, as shown in Figures 6 and 7. The pressure is monitored by a gauge in the vacuum line that measures pressures below 1 Torr. A vacuum is needed because air has the effect of slowing down α-particles and dispersing their energy. The detector gives its signal to the charge sensitive preamplifier. The main function of the preamplifier is to maximize the signal-to-noise ratio, which is why it is crucial to locate the preamplifier as close as possible to the detector. As the signal coming from the detector is very low, the preamplifier also serves as the first amplification stage [44]. The bias voltage of the detector is supplied to the High Voltage (HV) connection point on the preamplifier. The output signal of the preamplifier goes to the linear pulse-shaping amplifier. Its main function is to amplify and shape the amplitude signal from the preamplifier. The ORTEC Model 450 Research Amplifier has 100 shaping-time constant combinations [45]. The goal was to optimize the amplifier settings to get a well resolved α-spectrum for the different silicon detectors.

The amplifier output is connected to an ORTEC Multichannel Analyzer (EASY-MCA-8K), which in turn is connected to a computer with the MAESTRO software program. The MCA converts the incoming voltage pulses into a spectrum, distributing the number of counts over specific channels or bins. These channels are related to energy, and each channel corresponds to a certain voltage range. Hence, pulses with a voltage within this range, will end up in the same channel.

Two radioactive sources were used to test the detectors: an ^{241}Am alpha source and a ^{223}Ra ion source. A schematic overview of the experimental setups is shown in Figures 6 and 7 for the measurements with the ^{241}Am and ^{223}Ra source, respectively.

3.1.1   Schematic setup using ^{241}Am

The ^{241}Am source was placed inside a vacuum chamber, 2 cm above the detector. The schematic diagram of this experimental setup, and a picture of the design of the detection setup, is shown in Figure 6.
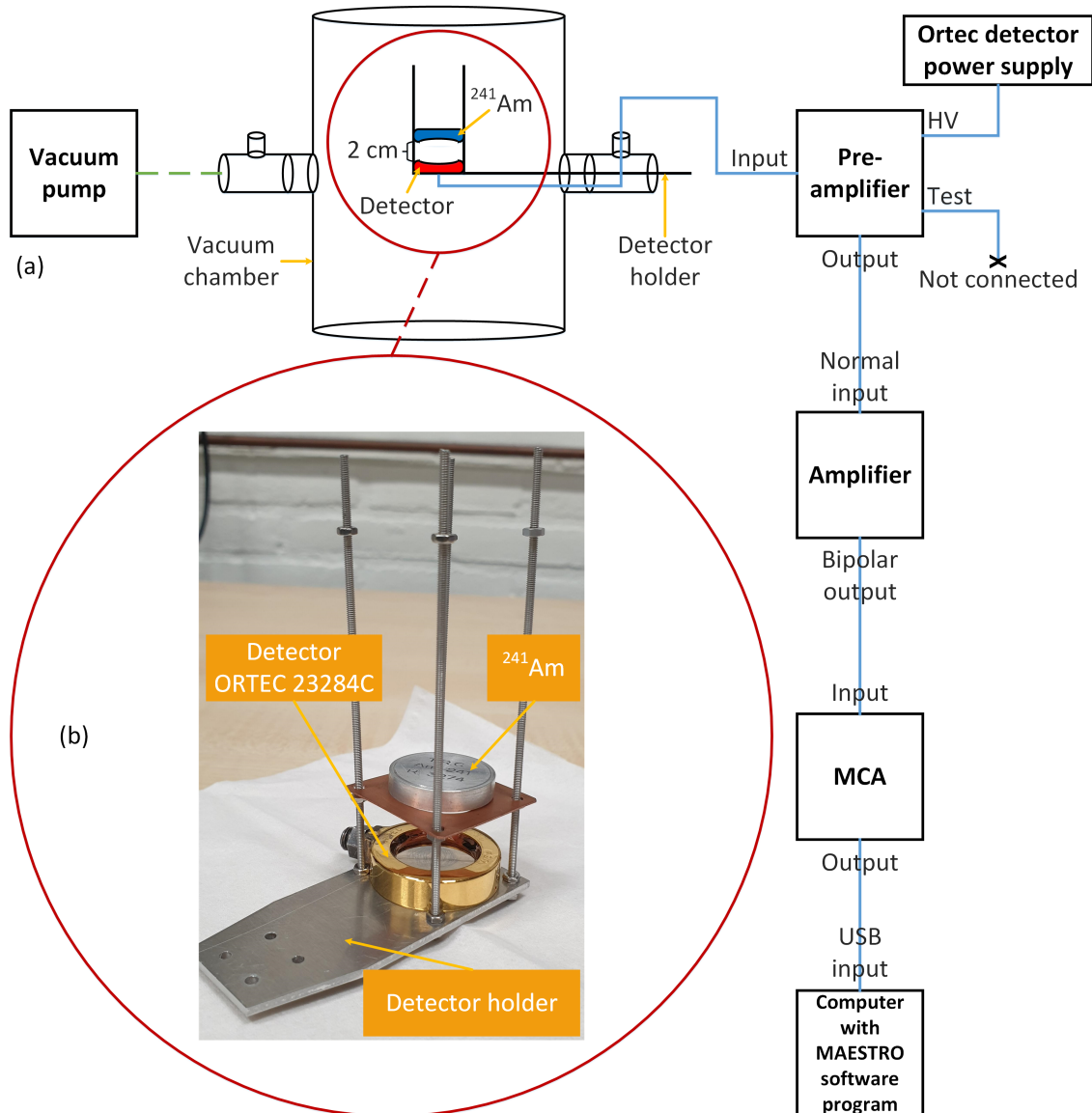
Figure 6: *(a) Schematic diagram of the test setup used to test the detector with an* ^{241}Am *source. The source was placed in a vacuum chamber,* $2\,\text{cm}$ *above the detector. The dashed green- and solid blue lines indicate the vacuum- and electric connections, respectively. (b) Picture of the design of the detection setup for the* ^{241}Am *source, which is installed in the vacuum chamber.*

3.1.2   Schematic setup using ^{223}Ra

For the measurements with the ^{223}Ra source, the setup was slightly modified (Figure 7). The distance between the source and the detector increased to 8.6 cm. Also, an ion catcher foil with a diameter of 22 mm was assembled 0.3 cm above the detector. A negative voltage was applied to the foil to attract the positively charged ions. This was done by connecting a cable to the foil in between the two plates made of polycarbonate.
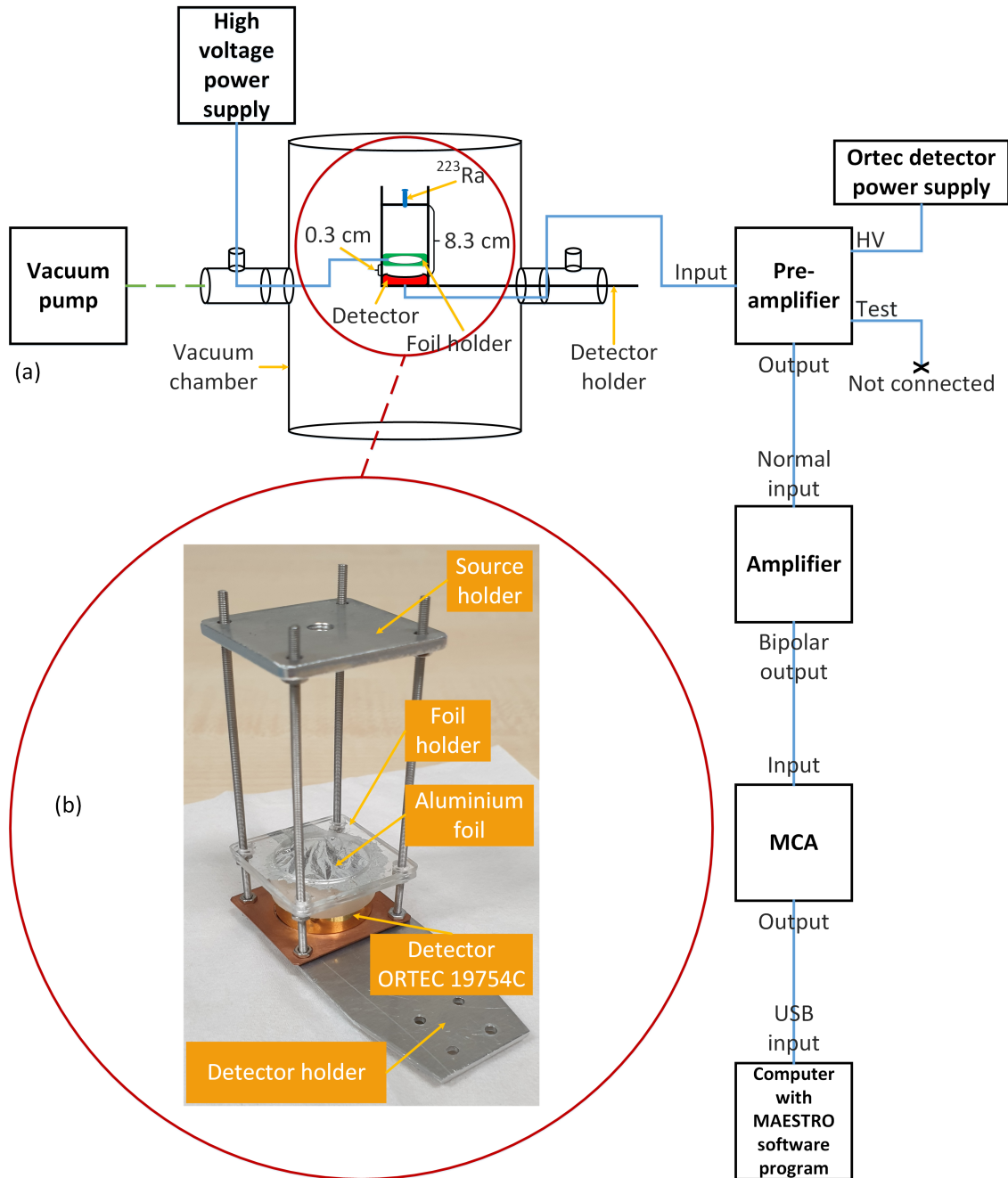
Figure 7: *(a) Schematic diagram of the test setup used to perform measurements with a ^{223}Ra source. The source was placed in a vacuum chamber, $8.6\,cm$ above the detector. In between, an ion catcher foil with a diameter of $22\,mm$ was assembled $0.3\,cm$ above the detector. The dashed green- and solid blue lines indicate the vacuum- and electric connections, respectively. (b) Picture of the design of the detection setup for the ^{223}Ra source, which is installed in the vacuum chamber. An M5 source screw was mounted on the top plate at $8.6\,cm$ distance from the detector.*

3.2   CISe setup

The schematic diagram of the CISe setup is shown in Figure 3. However, within this project, a detector holder was placed behind the carpet (Figure 11). Instead of the laser ablation source, a ^{223}Ra ion source (Section 2.2.2) was mounted inside the gas cell. This research has been conducted to examine if the ions can be extracted through the carpet by installing a silicon detector behind

the carpet. This section describes the function of the various components that are needed in the setup: the gas catcher, the electronics and the carpet, and the design of the detection system.

3.2.1 Gas catcher

The main function of the gas catcher is to slow down and guide the ions to the ion guide. Figure 8 shows the design of the gas catcher, including its main components. The gas catcher is operated at room temperature (293 K) and a helium pressure of $p_0 = 50$ mbar. The gas cell is filled with helium gas to slow down the ions. A dewar filled with liquid nitrogen surrounds the helium gas line, this is called a cold-trap. The cold-trap is used to decrease the amount of impurities in the helium by freezing them out. To monitor the pressure, two pressures gauges are connected: a digital pressure gauge and an analog pressure gauge. The digital pressure gauge is not calibrated for helium, but it is accurate for pressures up to $\sim 10^{-2}$ mbar. The analog pressure gauge is used to measure the pressures from 1 mbar.
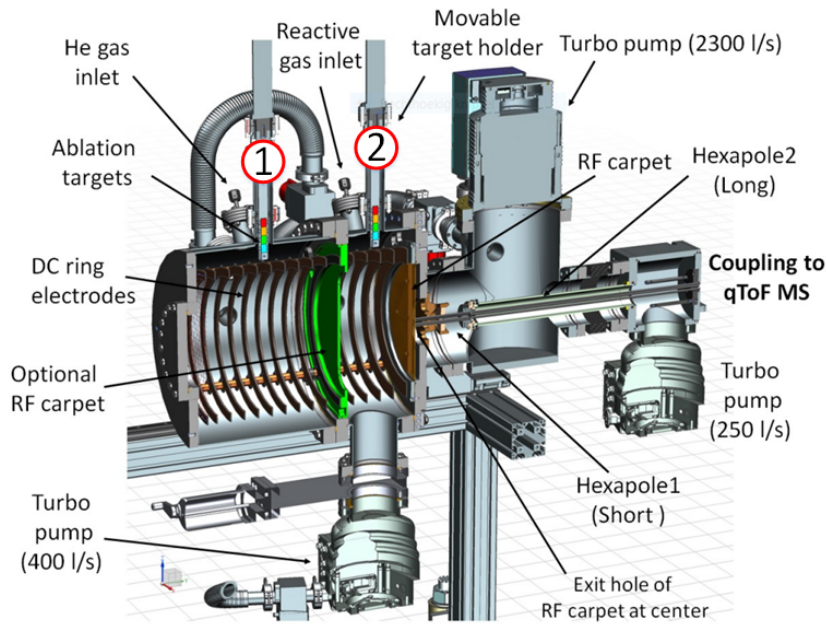

Figure 8: *Schematic overview of the gas catcher coupled to the ion guide. Figure adapted from Ref. [10]. The numbers circled in red indicate, in sequence, target holder #1 and target holder #2.*

A ^{223}Ra ion source is installed inside the gas catcher on target holder #2. These ions are guided towards the ion guide by an electrode system. This electrode system, shown in Figure 9, consists of DC ring electrodes (or DC cage) and a RF carpet that provides a RF- and DC field. The DC cage consists of 16 ring electrodes connected by equal resistors of $50\,\text{k}\Omega$ that create an electric field gradient, resulting in a gradual decrease in voltage. This means that the first ring (grid electrode) has the highest maximum voltage given by the power supply, while at the last ring, at the extraction side, a minimum voltage of $0\,\text{V}$ is applied. The metal wire at the grid electrode also prevents the ions from flying in the wrong direction. The result is that the ions are being guided to the extraction side of the gas catcher.
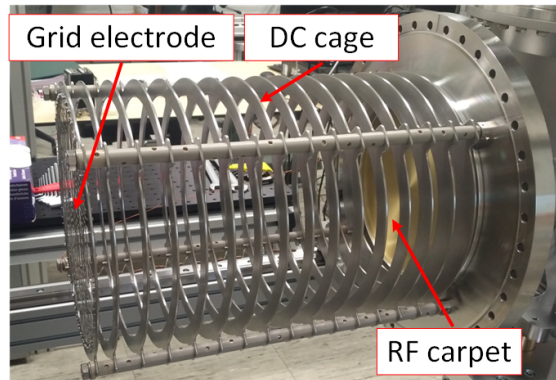

Figure 9: *Picture of the electrode system that helps guiding and extracting the ions from the gas cell. Figure adapted from Ref. [27]. The RF carpet is mounted at the extraction side of the gas catcher.*

3.2.2 RF carpet

The RF carpet is mounted at the extraction side of the gas catcher. The concentric ring electrodes have a phase difference of 180° between adjacent electrodes, and an electrode gap of 0.125 mm. The DC gradient of the carpet has the same function as the DC cage: a maximum voltage is applied to the outer ring electrode of the carpet, and a minimum voltage (0 V) to the ring electrode closest to the exit hole. A picture of the front- and the back side of the carpet is shown in Figure 10. The diameter of the carpet is 250 mm, and the extraction orifice has a diameter of 0.45 mm [27]. The working principle of the RF carpet is explained in Section 2.1.1.
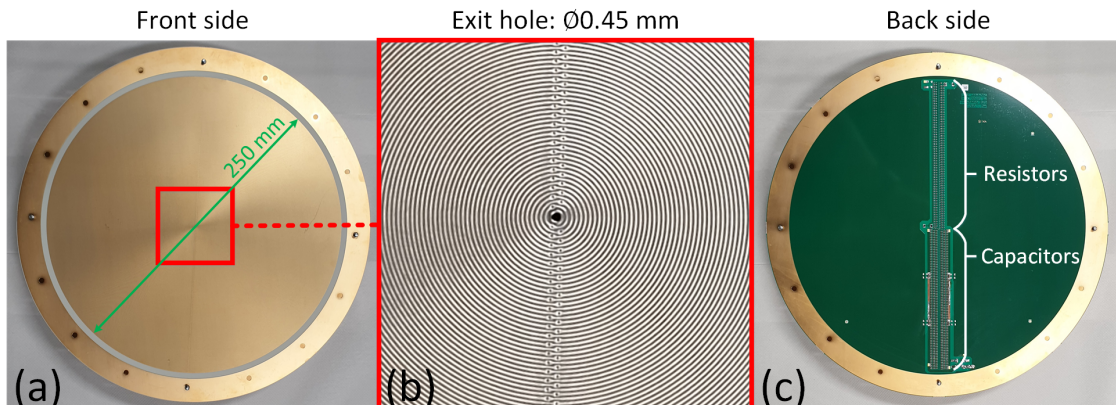

Figure 10: *Front- and back side pictures of the carpet. (a) Front side of the carpet, which has a total diameter of 280 mm. The electrode structure has a diameter of 250 mm. (b) Zoomed view of the front side of the carpet, showing the exit hole which has a diameter of 0.45 mm. Also evident is the concentric ring electrode structure. The gap between the electrodes is 0.125 mm. (c) Back side of the carpet, showing the electronic components consisting of resistors and capacitors.*

Simulations and first experiments were already performed to examine the ion guiding in the gas catcher and the ion extraction from the gas catcher to the ion guide. The ion trajectories in the vicinity of the exit hole of the RF carpet were simulated by B. Anđelić [27]. The DC gradient on the RF carpet was set to 3 V/cm. The results show a 100 % transmission, where the electric fields and gas-flow were included in the calculations [10]. In the first experiments, it was investigated if the ions, created by laser ablation, hit the carpet by using the carpet as a Faraday cup. The ions hitting the carpet are available for ion extraction. It was determined that the number of charges observed on the carpet ranges from $1.7 \cdot 10^8 e$ to $4.5 \cdot 10^{10} e$ [46].

Hence, according to the simulations, it should be possible to guide and extract the ions from the gas catcher using a RF carpet. And, according to first experiments, the ions are guided towards the carpet. The next experimental step to examine is if the ions are being extracted from the gas catcher to the ion guide. A detection system has been designed to perform these measurements, which is described in Section 3.2.3.

3.2.3 Design detection system

The setup used to perform the measurements within the CISe setup is shown in Figure 11(a). The important components are indicated. To install the detector inside the setup, a detector holder had to be designed. It had to fit inside the area behind the carpet, which has a length of 125 mm [12]. A holder for the detector, as well as for the foil, was needed. This resulted in the design shown in Figure 11(b) and 11(c). The holders for the detector and the foil were both made of PEEK (Polyether Ether Ketone), and the support ring was made of aluminium. The foil holder has a diameter of 9 mm. The length of the detector holder is 100 mm and the distance from the carpet to the foil holder is 8−10 mm. It was possible to change the distance between the detector- and the foil holder.
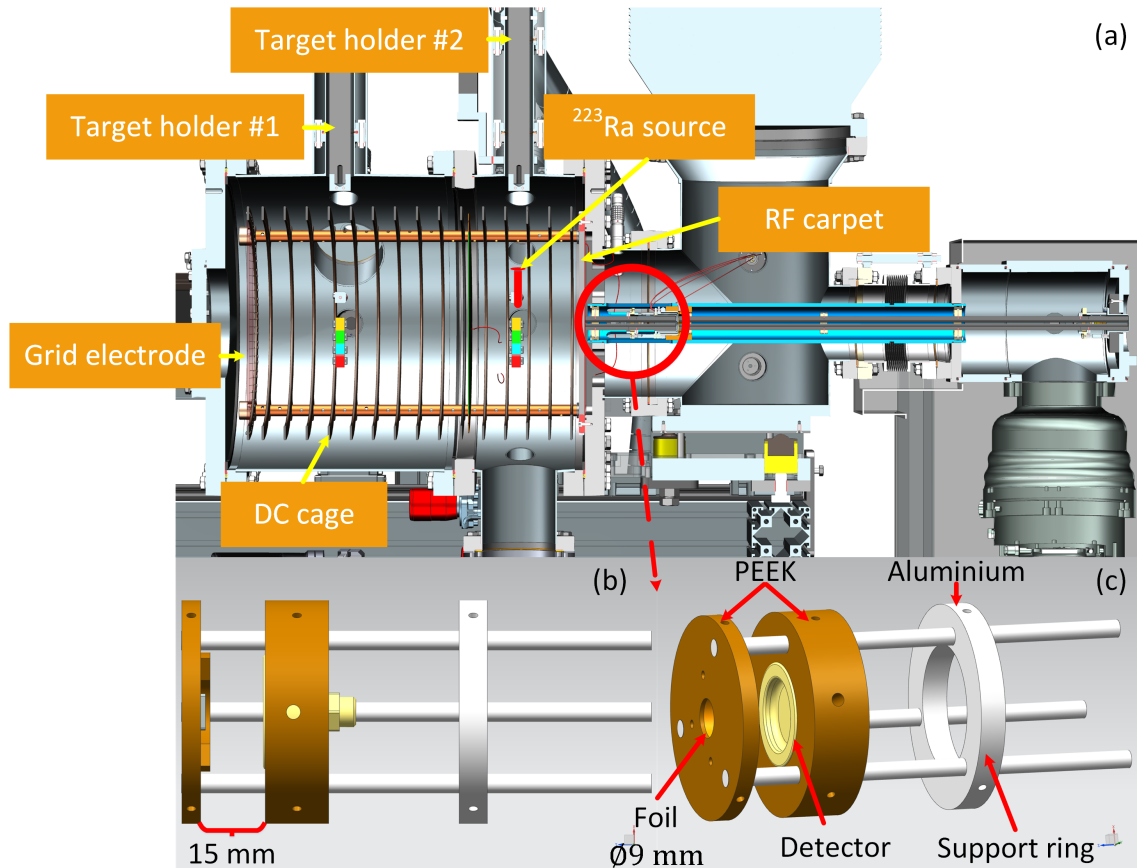
Figure 11: *(a) Setup for the detection of ions behind the carpet. The important components are indicated. A radioactive* ^{223}Ra *ion source was mounted inside the gas cell on target holder #2 and the designed detector holder, shown in (b) and (c), is placed behind the carpet. The holders for the detector and the foil were made of PEEK, and the support ring was made of aluminium. The foil holder has a diameter of* 9 mm. *The distance between the foil holder and the detector holder is, in this figure,* 15 mm.

The foil is mounted on non-conducting material, PEEK. A copper ring is connected to the foil so that it is possible to apply a voltage to the foil. Applying a negative voltage to the foil will result in the capture of the positive ions extracted from the gas catcher. This is realized by connecting a stripped cable to the copper ring, fixed in between the ring and the stainless steel cable clamp. The clasp made from PEEK is used to hold the ring in place. Figure 12 shows a picture of the design of the foil holder.
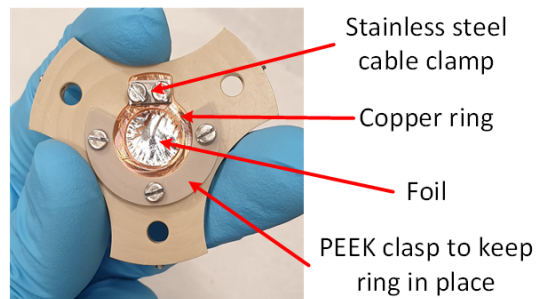
Figure 12: *Design of the foil holder. A cable will be clamped in between the small stainless steel plate and the copper ring, which is connected to the foil.*

The influence of various foils and meshes was examined, which is why the design of the detector holder changed between measurements. Figure 13 shows pictures of two different designs of the detector holder. The distance between the detector and the foil is 15 mm for both designs.

The first design, shown in Figure 13a, was used to test the various foils and meshes. The foil holder has material removed around the edges because of the gas flow. For the mesh there would not be a problem since the gas can flow through the holes from the mesh, but the gas cannot be evacuated through the foil. The detector holder also has material removed from its edges for the same reason.

After examining the foils and meshes, the second design was made with the idea to attract more ions using the aluminium mesh. A new foil holder was manufactured, closing the edges (Figure 13b). This allowed the gas to only pass through the middle hole, which will result in a higher extraction efficiency.
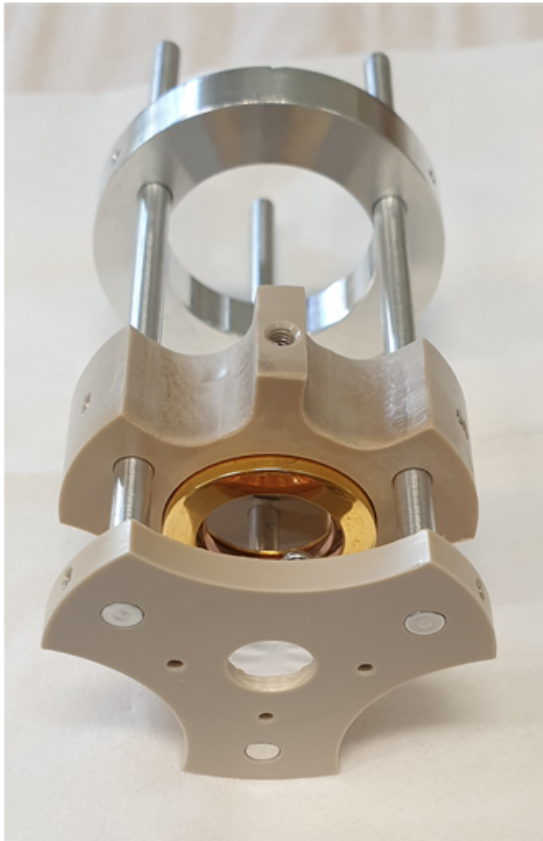
(a) Detector-foil: 15 mm.　　　　　　　　　(b) Detector-mesh: 15 mm.
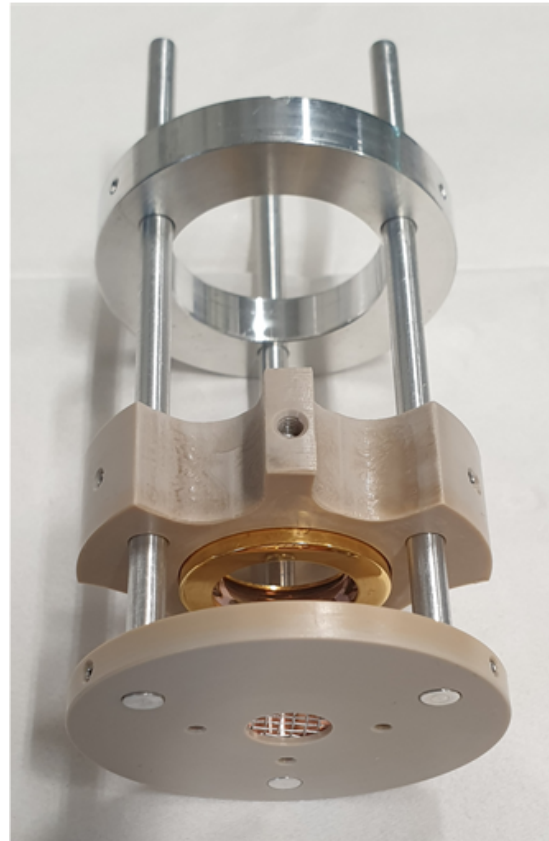
Figure 13: Two different designs of the detector holder.

4 Measurements and analysis

This research has been performed to examine the ion guiding and ion extraction from the gas catcher. The first measurements were done in a test setup, the results are shown and described in Section 4.1. The measurement results from the CISe setup are reported in Section 4.2. Lastly, Section 4.3 shows the results of the measurements of the DC gradient on the DC cage and the RF carpet.

4.1 Test setup

The goal of the test setup was to investigate various silicon detectors and optimize the settings to get a well resolved α-spectrum. The first step was to get familiar with the working principle of the detector and with the equipment in the setup. Three detectors were tested, two of them extensively because of the promising results. In this thesis, the focus was on these two detectors. The results are discussed in sections 4.1.1 and 4.1.2.

4.1.1 Detector ORTEC 23284C

Since the detectors used were old, they did not all come in the proper case where the specifications were written on. Hence, unfortunately, the specifications of this detector are not known. The results are subdivided into the radioactive sources that were used.

^{241}Am alpha source

The first measurements were performed with a radioactive ^{241}Am source. The setup for these measurements is shown in Figure 6. Different settings had to be adjusted to find a well resolved α-spectrum. Settings on the amplifier that had to be optimized were the gain factor, coarse and fine gain, and the shaping time constant. The shaping time constant consists of a low-pass filter called integrate, and a high-pass filter called differentiate. Besides, the bias voltage for the optimal performance of the detector had to be found.

The optimal bias voltage was found by performing several measurements for bias voltages between $50\,\mathrm{V}$ and $150\,\mathrm{V}$ in steps of $20\,\mathrm{V}$. It was determined that for a bias voltage of $70\,\mathrm{V}$, the performance of the detector was not increasing anymore.

Increasing the gain resulted in the peaks shifting to different channels, a broadening of the peaks, and a lower number of counts. The noise count rate also increased. Since this is as expected, it is concluded that the amplifier is working. An example of the measurement results for different fine gains is given in Figure 14.
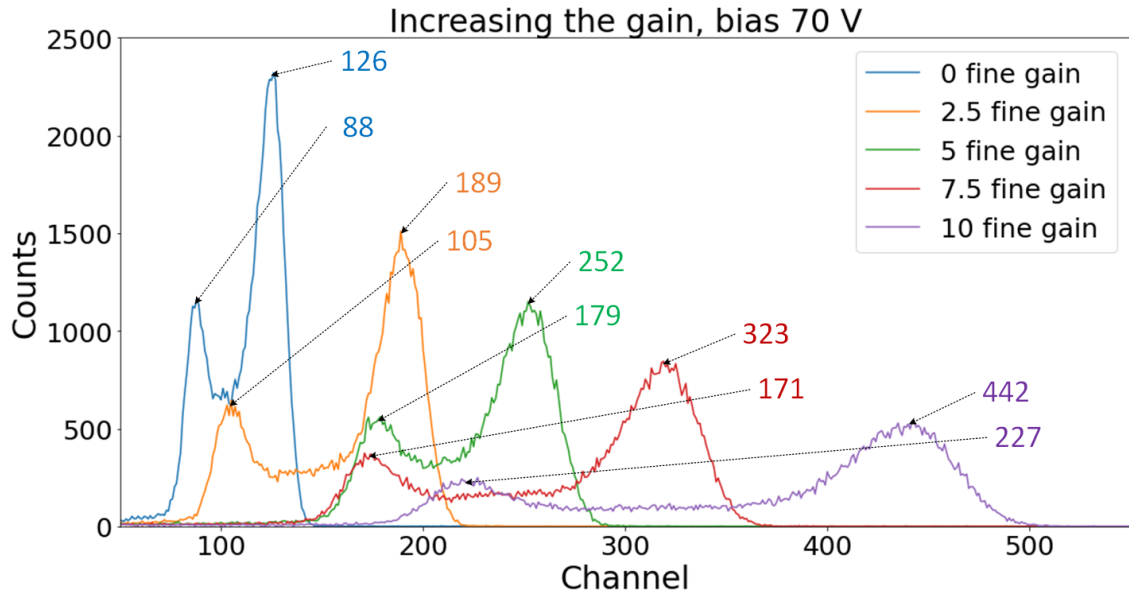
Figure 14: *Study of the influence of the amplifier gain on the measurements using an ^{241}Am source. Increasing the fine gain results in broader and lower peaks, and a shift of the peaks to different channels. The channel numbers at which the peaks occur are indicated in the figure. Note that this figure shows the raw measurement data. The lines are drawn to guide the eye.*

The shaping time constant also had to be optimized. Measurements for different combinations of the integrate and differentiate settings were performed. For this detector, integrate was set to 0.5 μs, and differentiate was also set to 0.5 μs. These settings were also used for the measurements shown in Figure 14.

An ^{241}Am source was used to test the detector. The goal was to find a well resolved α-spectrum by finding the optimal combination of the settings of the amplifier, and the bias voltage given to the detector. A compromise had to be made between the resolution of the peaks and the noise that is picked up by the detector. Increasing the gain resulted in an increase in the dead time, which is undesirable. The optimal settings for the amplifier were found when the gain was set to 200 coarse gain and 0 fine gain, and the shaping time constant was set to 0.5 μs integrate and 0.5 μs differentiate. The fitted α-spectrum of ^{241}Am is shown in Figure 15.
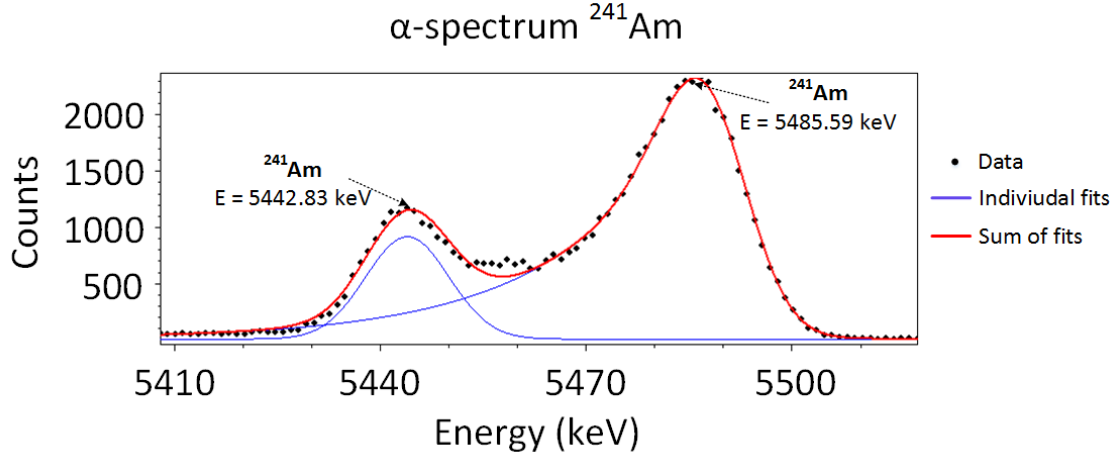
Figure 15: *Alpha-decay spectrum of ^{241}Am. The black dots correspond to the measured data points, the blue lines to the fit of the individual peaks, and the red line is the sum of the fit of the individual peaks. The fit function used is the alpha peak with 3 tails. The measurement time was* 2.5 min *with silicon detector ORTEC 23284C. The bin width is* 1.1253 keV.

The program used for the fitting is COLEGRAM [47]. The fit function used is the alpha peak with 3 tails. It is the sum of a Gaussian and three left-sided tails [48]:

$$ALPHA3(x) = G(x) + T_1(x) + T_2(x) + T_3(x) \tag{10}$$

where $G(x)$ and $T_i(x)$ ($i = 1, 2, 3$) are given by:

$$G(x) = A \cdot exp\left(-\frac{(x - x_0)^2}{2\sigma^2}\right)$$

$$T_i(x) = \frac{A \cdot T_i}{2} \cdot exp\left((x - x_0)\tau_i + \frac{\sigma^2 \tau^2}{2} \cdot \text{erf}\left(\frac{1}{\sqrt{2}}\left(\frac{x - x_0}{\sigma} + \sigma\tau_i\right)\right)\right)$$

where x_0 is the position, A the amplitude, σ the standard deviation, T_i ($i = 1, 2, 3$) the relative tail amplitude, and τ_i ($i = 1, 2, 3$) the exponential slope.

^{223}Ra ion source

After verifying the detector was properly working with an ^{241}Am source, measurements with a ^{223}Ra source were performed. The setup for these measurements is shown in Figure 7. Measurements without a foil, with 13 μm aluminium foil, and with 0.5 μm aluminium foil were performed. The peaks in the measured spectra are identified based on their α-energies and labelled according to the notation given in Table 2.

Measurements without a foil

For these measurements, the ion catcher foil is removed from the setup shown in Figure 7. The source-detector distance is 8.3 cm. The results are shown in Figure 16. For all measurements the bias voltage was set to 120 V, and the amplifier settings were set to 100 coarse gain, 4.5 fine gain, 0.25 μs integrate, and 0.5 μs differentiate.

The first measurement was performed with the ^{223}Ra source inside the vacuum chamber. This corresponds to the blue graph in Figure 16. The peaks from Bi II, Rn III, Bi I, and Rn I overlap. Rn II is expected to be inside the Bi I peak since the resolution is not good enough to distinguish this peak separately. However, the result shows that the detector is able to characterize most isotopes of the decay chain of ^{223}Ra. For more information about the decay chain of ^{223}Ra, see Table 2.

21

The first background measurement was performed by removing the radioactive ion source. This results in the disappearance of the ^{223}Ra peaks. The α-peaks from ^{219}Rn and ^{215}Po also disappear because of their short half-lives. The red graph in Figure 16 corresponds to the peaks of ^{211}Bi, which are still detected because of the long half-life of its β-decaying parent ^{211}Pb ($t_{1/2} = 36.1$ min).

A second background measurement has been performed 72 min after the first background measurement. The result is shown in green in Figure 16. From the activity of Bi I in background measurement 1 (red) and background measurement 2 (green), the half-life can be calculated. This is done by rewriting the radioactive decay law:

$$A = A_0 \cdot e^{-\lambda t} \tag{11}$$

$$= A_0 \cdot e^{-\frac{\ln(2)}{t_{1/2}}t} \tag{12}$$

to:

$$t_{1/2} = \frac{-\ln(2) \cdot t}{\ln\left(\frac{A}{A_0}\right)} \tag{13}$$

The activity of Bi I in background measurement 1 is measured to be $A_0 = 3.94 \pm 0.11$ cps, and in background measurement 2, $A = 0.95 \pm 0.06$ cps. The uncertainty in the activity is calculated with Equation 21, given in Appendix A.1. The time between the two background measurements was $t = 72$ min. With these values, the half-life is calculated to be $t_{1/2} = 35.08 \pm 1.63$ min. This corresponds to the half-life of ^{211}Pb, which is as expected. The equation for the calculation of the propagated error in the half-life is given in Appendix A.2 (Equation 25).
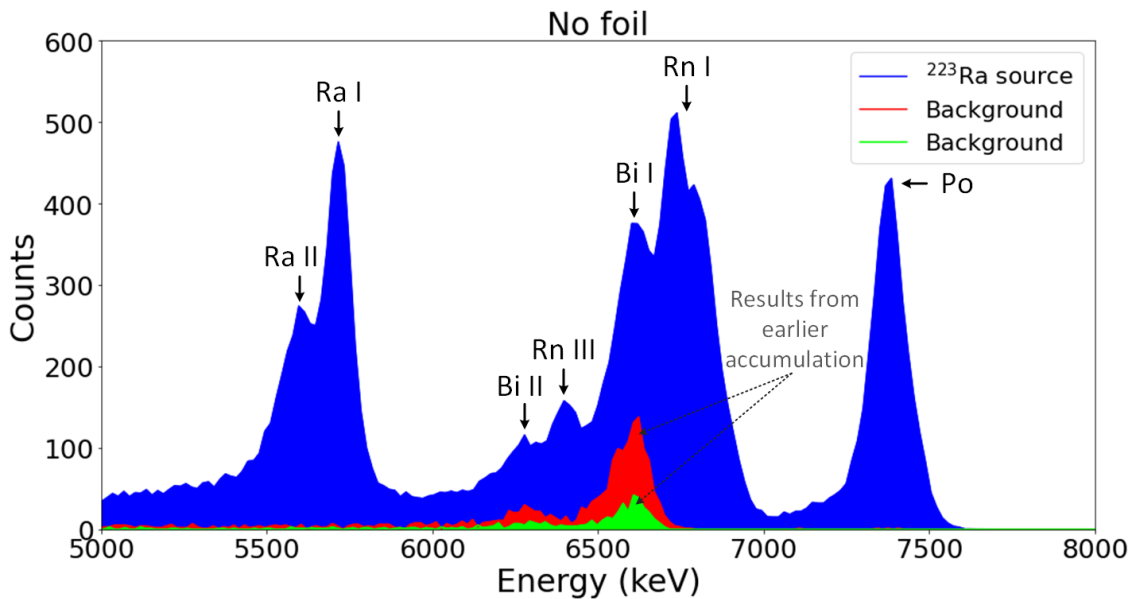
Figure 16: *Measured spectrum of the decay of* ^{223}Ra *for detector ORTEC 23284C (blue graph). The red- and green graphs represent the background measurements where the source was removed. The measured spectra correspond to the peaks of* ^{211}Bi*, which are still detected because of the accumulated* ^{211}Pb*. The measurement time was* 300 s*. The bin width is* 17.039 keV*. Note that this figure shows the raw measurement data. The lines are drawn to guide the eye.*

Measurements with an aluminium foil

For the next measurements, an aluminium ion catcher foil was installed in between the radioactive source and the detector. To study the influence of the aluminium foil, two measurements with a different foil thickness were compared to a measurement without a foil. Figure 17 shows the results.

The measurement without a foil, blue graph Figure 17, is included so that it can be compared to the foil measurements. The peaks are identified based on their α-energies and labelled according to the notation given in Table 2. The two measurements with the foil show a shift in energy. This is because ions propagating through a target material lose energy by ionization and excitation of atoms in the material, which is known as energy straggling. Due to this energy straggling, the resulting peaks have a broader energy distribution. The relation between the ion energy loss and the material thickness is known as the stopping power, dE/dx.

Figure 17 shows that the energy shift is much larger for the red graph than for the green graph. This means that the ions have to pass through more target material for the measurement that resulted in the red graph, thus, resulting in higher energy loss. The thickness of the foils can be calculated with the measured energy shift according to the following equation [49]:

$$d = \frac{\Delta E}{\left(\frac{dE}{dx}\right)_{E_0}} \tag{14}$$

where d is the thickness of the foil, ΔE is the measured energy loss, and $(dE/dx)_{E_0}$ is the total stopping power for the initial energy of the particle. It is assumed that the thickness of the material is much smaller than the particle range, $d \ll R$. Note that, due to microscopic inhomogeneities, the thickness of the aluminium foils will not be the same everywhere. Hence, the calculated foil thicknesses are an approximation.

The stopping power, dE/dx, can be calculated using the software package SRIM (Stopping and Range of Ions in Matter) [18]. The total stopping power has an electronic- and a nuclear stopping power contribution. The electronic stopping refers to the inelastic collisions between the incoming ion and the electrons in the target material. The nuclear stopping is due to the elastic collisions between the incoming ion and the nuclei in the target material.

The thickness of the aluminium foils is calculated by examining the energy shift of both the Ra I and Po peaks. The radium and polonium peaks are indicated for all three measurements in Figure 17. The energies of the blue, red, and green radium and polonium peaks are given in Table 3. The α-particle energy from the decay of ^{223}Ra and ^{215}Po is equal to 5716.23 keV and 7386.1 keV, respectively. For these energies, the electronic- and nuclear stopping power are calculated by SRIM. The results are given in Table 3.

Table 3: *Energies and stopping power in aluminium of the radium and polonium peaks.*

Energy (keV)	$E_{Ra,blue}$	$= 5716.232$
	$E_{Ra,red}$	$= 3672.836$
	$E_{Ra,green}$	$= 5738.204$
	$E_{Po,blue}$	$= 7386.104$
	$E_{Po,red}$	$= 5760.176$
	$E_{Po,green}$	$= 7408.076$
Stopping power (keV/µm)	$\left(\frac{dE}{dx}\right)_{elec,Ra}$	$= 1.502 \cdot 10^2$
	$\left(\frac{dE}{dx}\right)_{nucl,Ra}$	$= 1.067 \cdot 10^{-1}$
	$\left(\frac{dE}{dx}\right)_{elec,Po}$	$= 1.279 \cdot 10^2$
	$\left(\frac{dE}{dx}\right)_{nucl,Po}$	$= 8.538 \cdot 10^{-2}$

With the values given in Table 3, the thickness of the aluminium foil of the measurement that resulted in the red graph (Figure 17) is calculated to be:

$$d_{RaI} = \frac{5716.232 - 3672.836}{(1.502 \cdot 10^2) + (8.538 \cdot 10^{-2})}$$

$$\approx 13.6 \, \mu m$$

$$d_{Po} = \frac{7386.104 - 5760.176}{(1.279 \cdot 10^2) + (8.538 \cdot 10^{-2})}$$
$$\approx 12.7\,\mu m$$

$$d = \frac{d_{RaI} + d_{Po}}{2}$$
$$\approx 13\,\mu m$$

For the measurement result shown in green in Figure 17, the thickness of the aluminium foil is calculated to be $d \approx 0.2\,\mu m$.
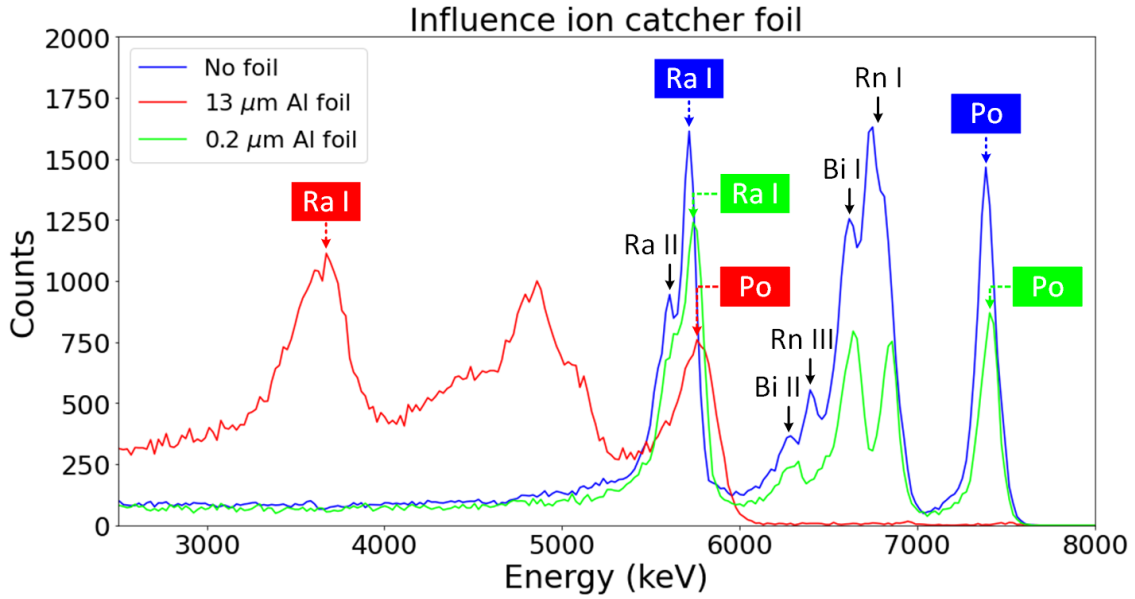

Figure 17: *Measured spectra of the decay of* ^{223}Ra *for detector ORTEC 23284C. The blue graph corresponds to the measurement without a foil. The red- and green graph correspond to the measurements where an aluminium foil was installed in between the source and the detector, the thickness of this foil was* $13\,\mu m$ *and* $0.2\,\mu m$, *respectively. The measurement time was* $900\,s$. *The voltage applied to the aluminium foils was* $-300\,V$. *The bin width is* $21.972\,keV$. *Note that this figure shows the raw measurement data. The lines are drawn to guide the eye.*

As shown in Figure 17 (red graph), ions passing through 13 µm aluminium foil lose a lot of energy. The peaks broaden and have more overlap with the other ions measured, resulting in a decrease of the peak resolution. It is not possible to distinguish all the peaks as in the measurement without a foil. Hence, it can be concluded that the 13 µm aluminium foil is too thick to measure the ^{223}Ra decay spectrum.

The energy shift of the measurement where 0.2 µm aluminium foil is employed, is very small. This is due to the small amount of target material the ions have to traverse. It was expected to detect the peaks at slightly lower energies compared to the measurement without a foil. However, as shown in Figure 17 (green graph), the peaks shifted to higher energies. It is possible that the detector calibration shifted, resulting in the peaks at higher energies.

It is still possible to differentiate the peaks of the measurement where 0.2 µm aluminium foil was used. The resolution between Rn I and Bi I is even better compared to the measurement without a foil. A more extensive study on the different foils is performed in the CISe setup, which is described in Section 4.2.1.

4.1.2 Detector ORTEC 19754C

The specifications of this detector are BA-24-150-1500. The numbers correspond to energy resolution, active area, and depletion depth, respectively. The A indicates that it is a partially depleted silicon surface barrier radiation detector, and the B stands for a B mount, where there is a microdot connector on the rear of the detector.

An extensive study of the influence of the amplifier settings and the bias voltage on the α-spectrum was performed using detector ORTEC 19754C. This was done with a ^{223}Ra ion source. The results show that the settings for the integrate and differentiate on the amplifier demonstrate a well resolved α-spectrum when they are both equal to 1 µs or both equal to 1.5 µs. The settings of the gain are equal to 200 coarse gain and 0 fine gain. Measurements were performed without a foil in between the source and the detector. The optimal settings were found to be 100 V for the bias voltage, and integrate and differentiate were set to 1 µs. The result is shown in Figure 18.
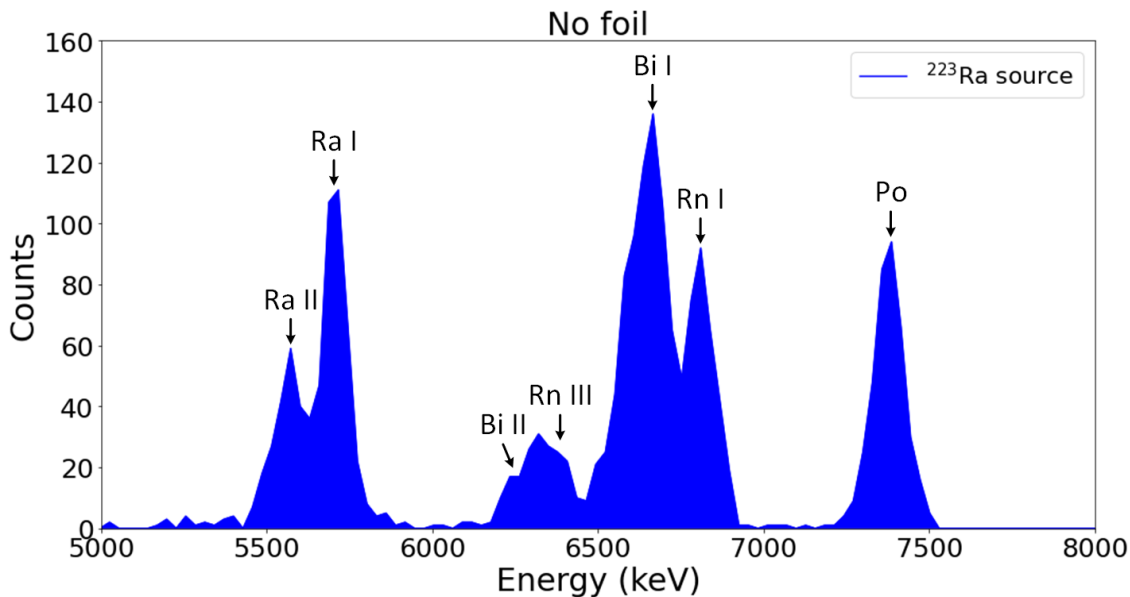
Figure 18: *Measured spectrum of the decay of ^{223}Ra for detector ORTEC 19754C. The bin width is 28.791 keV. Note that this figure shows the raw measurement data. The lines are drawn to guide the eye.*

The spectrum shown in Figure 18 shows that the Ra II, Ra I, Bi I, Rn I, and Po peaks are easily distinguishable, even though the bin width of 28.791 keV is quite large. Rn II is expected to be inside the Bi I peak since the resolution is not good enough to distinguish this peak separately. Compared to the α-spectrum of detector ORTEC 23284C shown in Figure 16 (blue graph), the peaks for Rn III and Bi II appear to have a worse resolution measured with detector ORTEC 19754C. They are both inside the broadened peak as indicated in Figure 18. However, the measurement result shows that the detector is able to resolve the most important isotopes of the decay chain of ^{223}Ra.

4.1.3 Conclusion

In the test setup, the α-spectra of two silicon detectors were studied. Both detectors produced a well resolved α-spectrum. The next step is to perform measurements in the CISe setup, where the detector is installed behind the RF carpet as shown in Figure 11(a). For this, detector ORTEC 19754C was selected to mount inside the CISe setup because of its smaller size and its easier mounting principle.

4.2 CISe setup

The goal was to examine if ions were extracted from the gas catcher by installing a silicon detector behind the RF carpet. Installing the detector was realized by designing a detector holder. The design of this holder is shown in Figure 11(b) and Figure 11(c). The setup used for these measurements is shown in Figure 11(a).

The first measurements were performed with a Source Place Holder (SPH) that replaces the carpet. The plate has a diameter of $280\,\text{mm}$, and a thickness of $\sim 5\,\text{mm}$. The middle of the plate has a tapped hole to mount an M5 source screw. For these measurements, the distance from the source to the detector is $23 - 25\,\text{mm}$. Different foils and meshes were tested using the SPH, where the foil holder was installed $8 - 10\,\text{mm}$ behind the plate. The results are given in Section 4.2.1. The foil or mesh with the best performance was used for the carpet measurements. Before these carpet measurements, the optimal settings were determined using the source plate, of which the result is shown in Section 4.2.2. The results for the carpet measurements are described in Section 4.2.3.

4.2.1 Testing various foils and meshes

The working of different foil- and mesh materials was examined at pressures of $\sim 10^{-2}\,\text{mbar}$. The goal of the ion capture foil is to capture the ^{219}Rn ions. The influence of applying a negative voltage to the foil is investigated by comparing this measurement to the measurement where $0\,\text{V}$ was applied to the foil. It is expected to see an increase in the number of counts for the ^{219}Rn peaks, which will then also lead to an increase of the peaks of ^{215}Po and ^{211}Bi. The foil measurements are also compared to the measurement without a foil. This is done to determine the energy shift so that the thickness of the foil could be calculated. The energy shift of both the Ra I and Po peaks have been taken into account for the foil thickness calculation. The design of the detector holder used for these measurements is shown in Figure 13a. The bias voltage of the detector for these measurements was $30\,\text{V}$.

Aluminium foil

The measurement result for the aluminium foil is shown in Figure 19. Compared to the measurement without a foil, the peaks for Po, Rn I, Bi I, and Bi II have less counts. This is due to the energy straggling of the positive ions with the electrons from the target material, ions can get lost in the foil. The thickness of the aluminium foil is calculated to be $\sim 1.3\,\mu\text{m}$, using Equation 14 and the values of the variables given in Table 4.

Table 4: *Energies and stopping power in aluminium of the radium and polonium peaks.*

Energy (keV)	$E_{\text{Ra,blue}}$	$= 5716.252$
	$E_{\text{Ra,red}}$	$= 5543.506$
	$E_{\text{Po,blue}}$	$= 7386.13$
	$E_{\text{Po,red}}$	$= 7213.384$
Stopping power (keV/μm)	$\left(\frac{dE}{dx}\right)_{\text{elec,Ra}}$	$= 1.502 \cdot 10^{2}$
	$\left(\frac{dE}{dx}\right)_{\text{nucl,Ra}}$	$= 1.067 \cdot 10^{-1}$
	$\left(\frac{dE}{dx}\right)_{\text{elec,Po}}$	$= 1.279 \cdot 10^{2}$
	$\left(\frac{dE}{dx}\right)_{\text{nucl,Po}}$	$= 8.538 \cdot 10^{-2}$

Figure 19 shows that there is no difference between the measurements where $0\,\text{V}$ (red graph) and $-1000\,\text{V}$ (green graph) was applied to the foil. The small increase in the Rn I peak is due to statistical fluctuations. It was not possible to apply a lower voltage to the foil, as this resulted in a breakdown voltage.
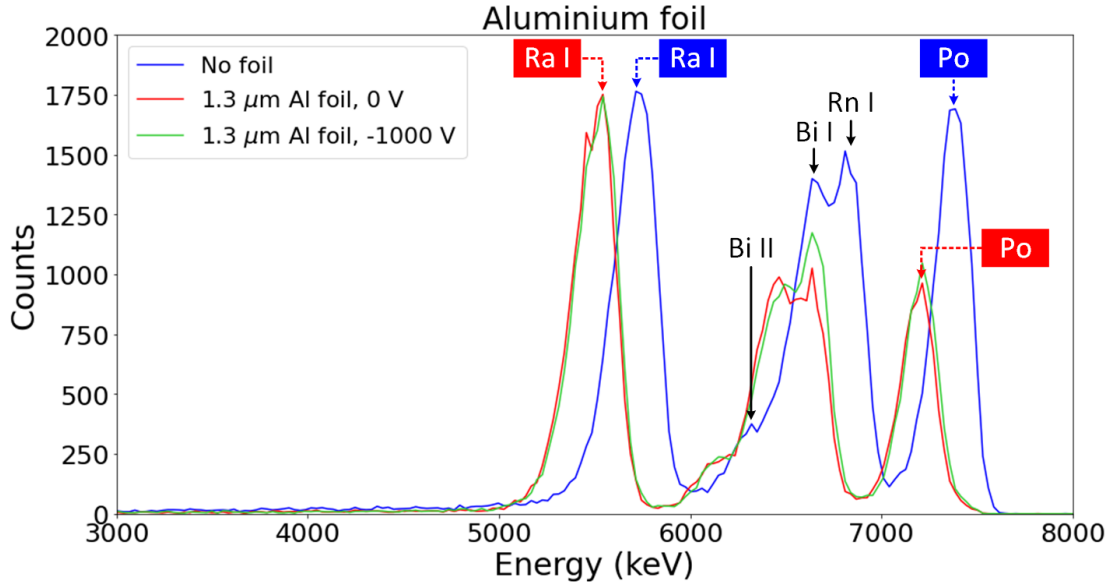
Figure 19: *Examining the influence of the aluminium foil. The blue graph indicates the measurement without a foil, the red- and green graphs correspond to the measurements where $0\,\mathrm{V}$ and $-1000\,\mathrm{V}$ was applied to the aluminium foil, respectively. The measurement time was $1800\,\mathrm{s}$. The bin width is $28.791\,\mathrm{keV}$. Note that this figure shows the raw measurement data. The lines are drawn to guide the eye.*

Aluminized mylar foil

When the carpet is in place, the foil holder is close to its extraction orifice. Aluminium foil is fragile due to the gas flow from the gas cell to the ion guide section. Aluminized mylar foil is mechanically more stable. It is more flexible than aluminium foil, and therefore less prone to tearing. The mylar foil has a small layer of aluminium on both sides. To make sure the negative voltage is applied to both sides of the foil, a small piece of aluminium foil connects the two parts. The measurement result for the aluminized mylar foil is shown in Figure 20.

The mylar foil measurements also show a decrease in the number of counts compared to the measurement without a foil, which means part of the ions are lost. The thickness of the aluminized mylar foil is calculated to be $\sim 6\,\mu\mathrm{m}$, using Equation 14 and the values of the variables given in Table 5.

Table 5: *Energies and stopping power in mylar of the radium and polonium peaks.*

Energy	$E_{\mathrm{Ra,blue}}$	$= 5716.252$
(keV)	$E_{\mathrm{Ra,red}}$	$= 5082.85$
	$E_{\mathrm{Po,blue}}$	$= 7386.13$
	$E_{\mathrm{Po,red}}$	$= 6839.101$
Stopping power	$\left(\frac{dE}{dx}\right)_{\mathrm{elec,Ra}}$	$= 1.011 \cdot 10^2$
(keV/μm)	$\left(\frac{dE}{dx}\right)_{\mathrm{nucl,Ra}}$	$= 6.865 \cdot 10^{-2}$
	$\left(\frac{dE}{dx}\right)_{\mathrm{elec,Po}}$	$= 8.389 \cdot 10^1$
	$\left(\frac{dE}{dx}\right)_{\mathrm{nucl,Po}}$	$= 5.474 \cdot 10^{-2}$

Figure 20 shows that there is no difference between the measurements where $0\,\mathrm{V}$ (red graph) and $-1000\,\mathrm{V}$ (green graph) was applied to the foil. For the aluminized mylar foil it was also not possible to apply a lower voltage to the foil, as this resulted in a breakdown voltage.

The small peak with the same energy as the Po peak of the measurement without a foil is most likely from a pinhole in the foil. Some of the α-particles do not "see" the foil and, as a result, do not lose (part of) their energy to the foil. Hence, these particles are detected in the same channel as the measurement without a foil in between the source and the detector.
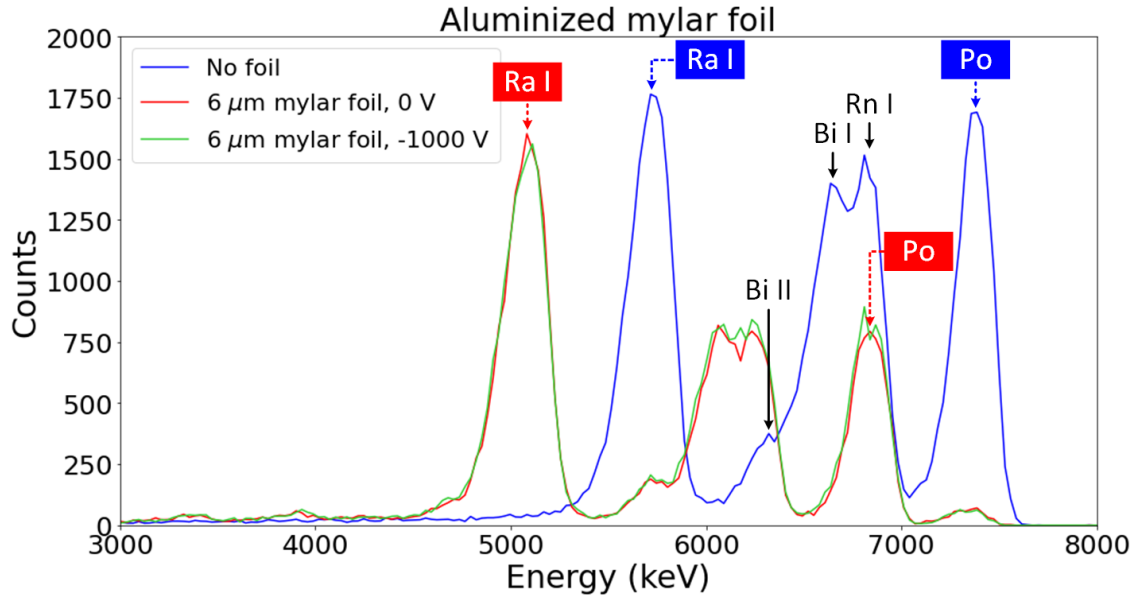

Figure 20: *Examining the influence of the aluminized mylar foil. The blue graph indicates the measurement without a foil, the red- and green graphs correspond to the measurements where $0\,\mathrm{V}$ and $-1000\,\mathrm{V}$ was applied to the aluminized mylar foil, respectively. The measurement time was $1800\,\mathrm{s}$. The bin width is $28.791\,\mathrm{keV}$. Note that this figure shows the raw measurement data. The lines are drawn to guide the eye.*

Stainless steel mesh

The stainless steel and aluminium meshes were tested because the foils did not give the desired results. The measurement result for the stainless steel is shown in Figure 21. The size of the holes in the stainless steel mesh is $\sim 0.1\,\mathrm{mm}$. Due to the holes in the mesh, there is no measured energy shift: the peaks appear in the same channel as the measurement without a foil. Hence, the wire thickness of the mesh is determined with a caliper, and it is measured to be $\sim 0.07\,\mathrm{mm}$.

It is apparent that a large amount of the α-particles are lost in the mesh compared to the measurement without a foil. Figure 21 also shows a small increase in the number of counts in the Rn I peak for the measurement where $-1000\,\mathrm{V}$ was applied to the mesh compared to the applied $0\,\mathrm{V}$ measurement. However, it was possible to apply a lower voltage to the stainless steel mesh compared to the aluminized mylar- and aluminium foil that were tested. So, another measurement was performed where $-2000\,\mathrm{V}$ was applied to the mesh. This resulted in another small increase with respect to the measurement where $-1000\,\mathrm{V}$ was applied to the mesh.
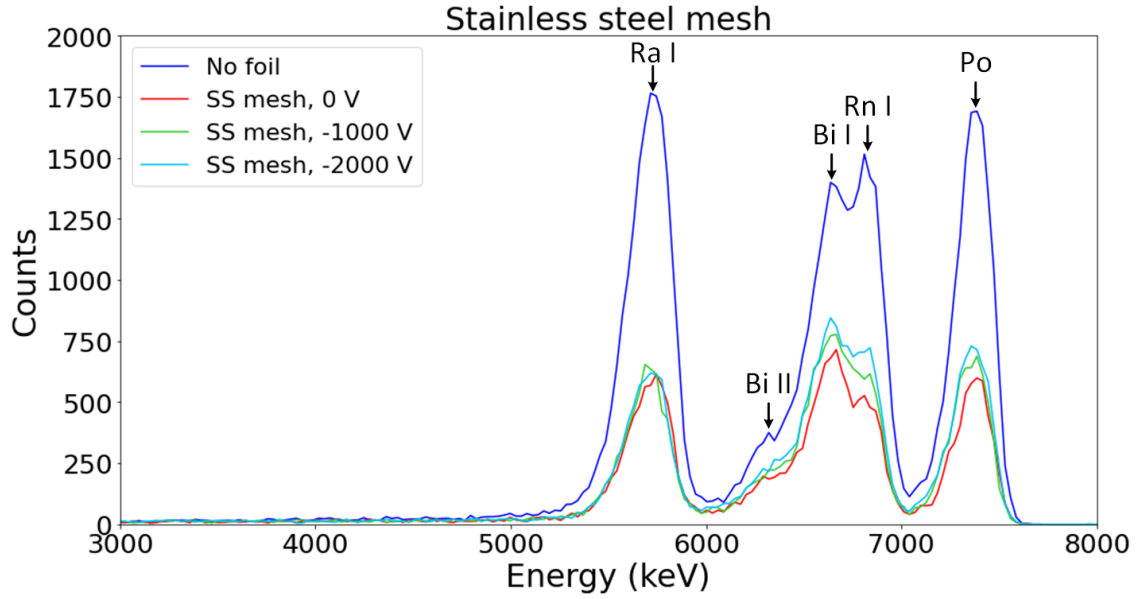
Figure 21: *Examining the influence of the stainless steel mesh. The blue graph indicates the measurement without a foil, the red-, green-, and light blue graphs correspond to the measurements where 0 V, −1000 V, and −2000 V were applied to the stainless steel mesh, respectively. The measurement time was 1800 s. The bin width is 28.791 keV. Note that this figure shows the raw measurement data. The lines are drawn to guide the eye.*

Aluminium mesh

The spectrum obtained with the aluminium mesh is shown in Figure 22. The size of the holes in the aluminium mesh is ∼ 1.5 mm. The wire thickness of the mesh is determined with a caliper and is measured to be ∼ 0.26 mm. The aluminium mesh has larger holes compared to the stainless steel mesh, which resulted in a smaller loss in the number of counts compared to the measurement without a foil.

For the aluminium mesh, there is a significant increase in the number of counts for Rn I, and therefore also for the bismuth and polonium peaks, as shown in Figure 22. Applying −1000 V to the aluminium mesh already resulted in a higher peak for Rn I, which was not the case for the tested foils. This increase is also higher compared to the stainless steel mesh. For the aluminium mesh it was also possible to apply lower voltages to the mesh. The measurement result where −2000 V was applied to the mesh is shown in light blue, Figure 22. It shows an even further increase of the α-particles detected in the Rn I peak.
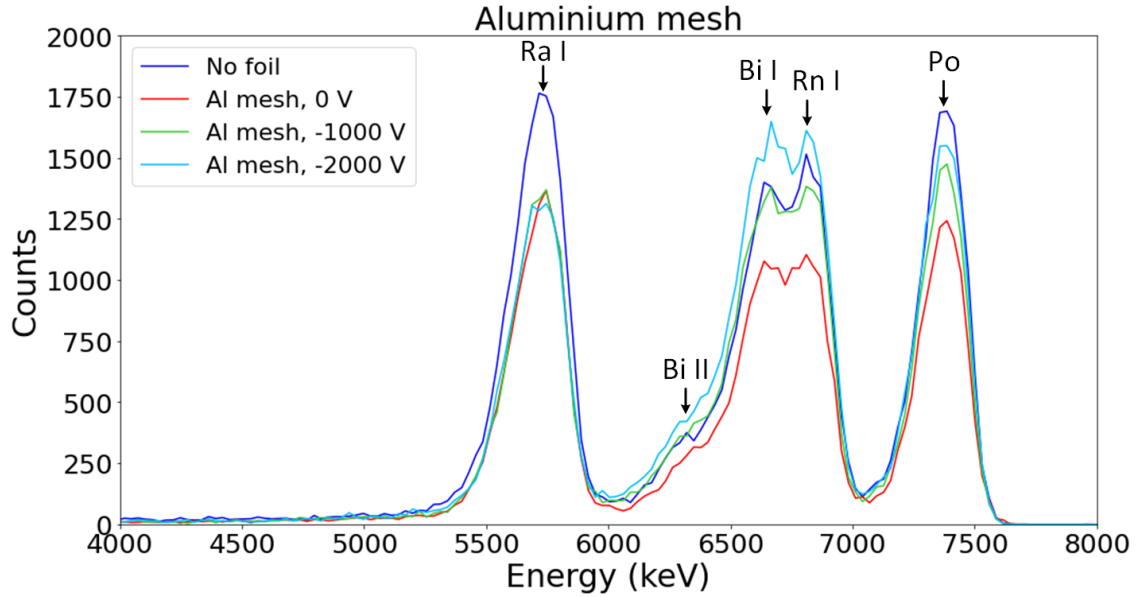
Figure 22: *Examining the influence of the aluminium mesh. The blue graph indicates the measurement without a foil, the red-, green-, and light blue graphs correspond to the measurement where 0 V, −1000 V, and −2000 V were applied to the aluminium mesh, respectively. The measurement time was 1800 s. The bin width is 28.791 keV. Note that this figure shows the raw measurement data. The lines are drawn to guide the eye.*

Conclusion

Four different ion capture materials were tested to determine which one had the best performance. The idea is to capture the ^{219}Rn ions, leading to an increase in the number of counts. This was studied by comparing measurements where a high negative voltage was applied to the foil/mesh to measurements where 0 V was applied to the foil/mesh. As shown in Figures 19 and 20, the foils did not show an increase in the number of counts of the Rn I peak when a negative voltage was applied to the foil. It is possible that the applied negative voltage was not high enough, but −1000 V was the maximum obtainable voltage due to the breakdown. The meshes on the other hand did show a significant increase in the number of counts in the Rn I peak when a negative voltage was applied. For the stainless steel mesh, Figure 21, this increase is smaller than for the aluminium mesh, Figure 22. The measurement with the stainless steel also had a greater loss of α-particles. Hence, it can be concluded that the aluminium mesh had the best performance, and this will be used for the carpet measurements.

4.2.2 Source plate holder measurements

The performance of the detector can change between measurements. As seen in Figure 22, not all the peaks are distinguishable. So, to get a well resolved α-spectrum, the bias voltage of the detector was modified to find the optimal setting. This was found to be 70 V. The result is shown in Figure 23. A voltage of −2500 V was applied to the aluminium mesh. The fit function used is the alpha peak with 3 tails, see Equation 10. The energies of the peaks are indicated in the figure, which are in good correspondence with the energies given in Table 2.
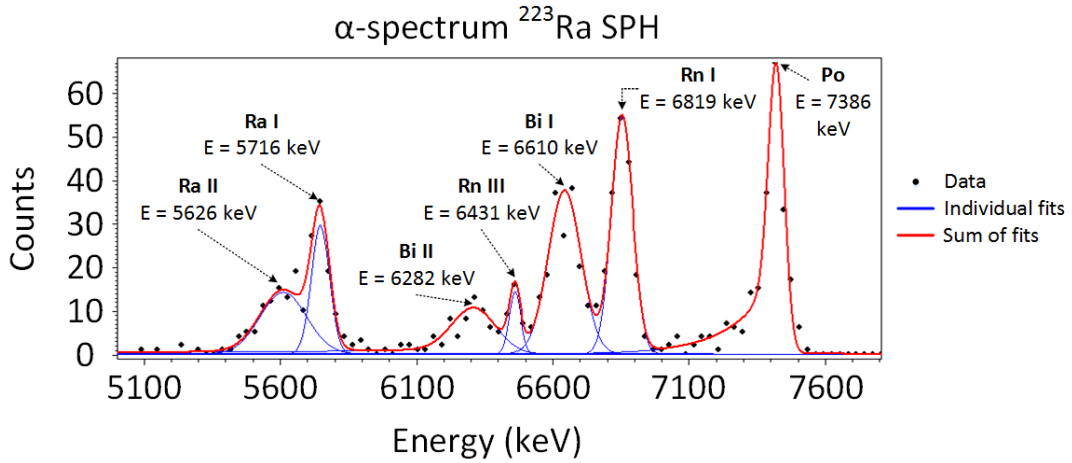
Figure 23: *Alpha-decay spectrum of* ^{223}Ra *from the source plate holder (SPH) measurement. The black dots correspond to the measured data points, the blue lines to the fit of the individual peaks, and the red line is the sum of the fit of the individual peaks. The fit function used is the alpha peak with 3 tails. The measurement time was* 900 s *with silicon detector ORTEC 19754C. The bin width is* 29.819 keV.

4.2.3   Carpet measurements

For the carpet measurements, the radioactive ion source, ^{223}Ra, was placed on target holder #2, shown in Figure 11(a). A similar spectrum as shown in Figure 23, without the ^{223}Ra peaks, is expected. The ^{223}Ra decays in the gas cell, so this will not be detected. However, as shown in Figure 24, only two peaks were measured. The fit function used is the alpha peak with 3 tails, see Equation 10. The voltages applied to the DC electronics are -3000 V to the aluminium mesh, 300 V to the DC cage, 0 V to the DC carpet, and 50 V to the target holder.
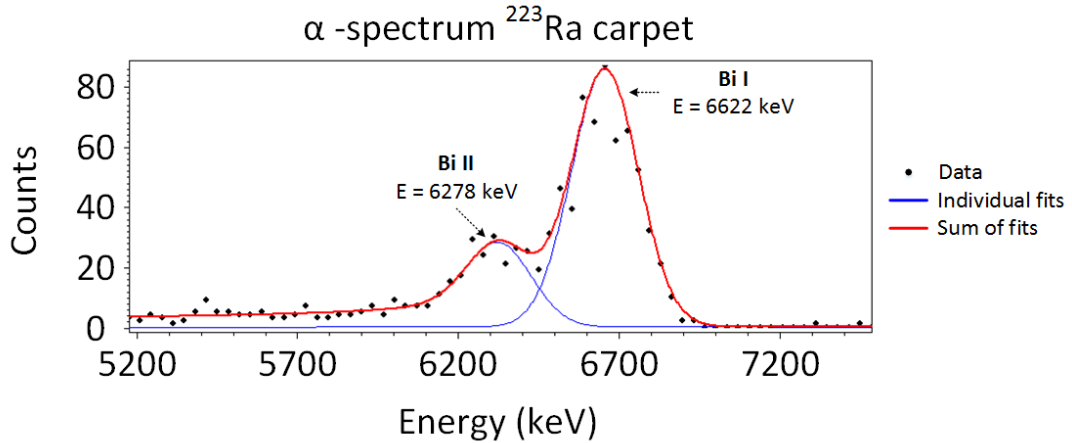
Figure 24: *Alpha-decay spectrum of* ^{223}Ra *from the carpet measurement. The black dots correspond to the measured data points, the blue lines to the fit of the individual peaks, and the red line is the sum of the fit of the individual peaks. The fit function used is the alpha peak with 3 tails. The measurement time was* 900 s *with silicon detector ORTEC 19754C. The bin width is* 34.47 keV.

The peaks that were measured, were identified as the two bismuth peaks, Bi I and Bi II (Figure 24). This was in the first place determined by taking the source out and performing another measurement. The two peaks were still present, which means they do not correspond to the ^{219}Rn ($t_{1/2} = 3.96$ s) and ^{215}Po ($t_{1/2} = 1.78$ ms) peaks because of their short decay times.

After the carpet measurements, another source plate measurement was performed so that the two measurements could be compared. The results are shown in Figure 25. Overlaying the carpet measurement (Figure 24) with the measurement performed in the source plate holder (SPH), also shows that the measured peaks correspond to bismuth. The bismuth peaks of the carpet measurement are not as sharp as the peaks from the SPH measurements due to the lower count rate, but the peaks can be attributed to ^{211}Bi.

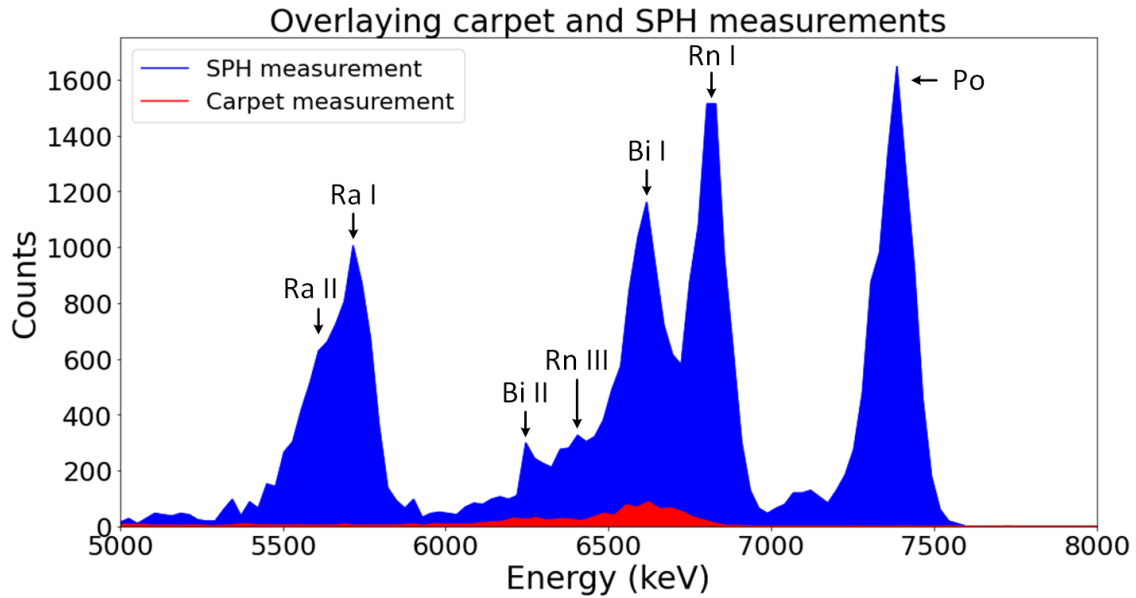Figure 25: *Overlaying the carpet measurement with the source plate holder measurement. It shows that the peaks from the carpet measurement (red) correspond to the bismuth peaks. The measurement time was* 900 s. *Note that this figure shows the raw measurement data. The lines are drawn to guide the eye.*

The half-life of the peaks can be determined to support the idea of the peaks corresponding to bismuth. Usually, this is done by a measuring device, reporting each time a count is detected in a specific channel. However, in this study, the decay rate was determined by a rough estimation. After removing the source from the gas cell, the activity was determined by performing eight short measurements. The activity is the average value over the whole measurement time. Table 6 shows the measured activities at specific times and their errors.

Table 6: *Measured activities at specific times for the decay rate study. The calculated errors are also given.*

Time (min)	Measurement time (s)	Measured activity (cps)	Vertical standard deviation (cps)	Horizontal standard deviation (min)
19.65	505	0.39	0.0278	8.42
28.87	505	0.31	0.0248	8.42
38.00	505	0.30	0.0244	8.42
69.40	505	0.16	0.0178	8.42
139.77	505	0.02	0.0063	8.42
206.15	1010	0.01	0.0031	16.83
224.38	1000	0.01	0.0032	16.67
242.85	1035	0.01	0.0031	17.25

At $t = 0$, the source was removed from the gas cell. "Time" in Table 6 is the time that has passed after taking the source out plus the measurement time. After 12 min, the first measurement was performed. Hence, it is assumed that all the detected ^{211}Bi comes from the decay of ^{211}Pb

from the mesh. Five measurements of 505 s, and three measurements of 1010 s, 1000 s, and 1035 s were performed. At these times, the activities were written down. The total measurement time is taken as the horizontal error. The vertical error is calculated with Equation 21, where t is the measurement time. The data points are fitted to the exponential radioactive decay law function, see Equation 11. The result is shown in Figure 26 (blue dotted line). Since the activity is the average value over the whole measurement time, the uncertainty in the activity is probably larger. However, here it was assumed it follows the Poisson distribution law.
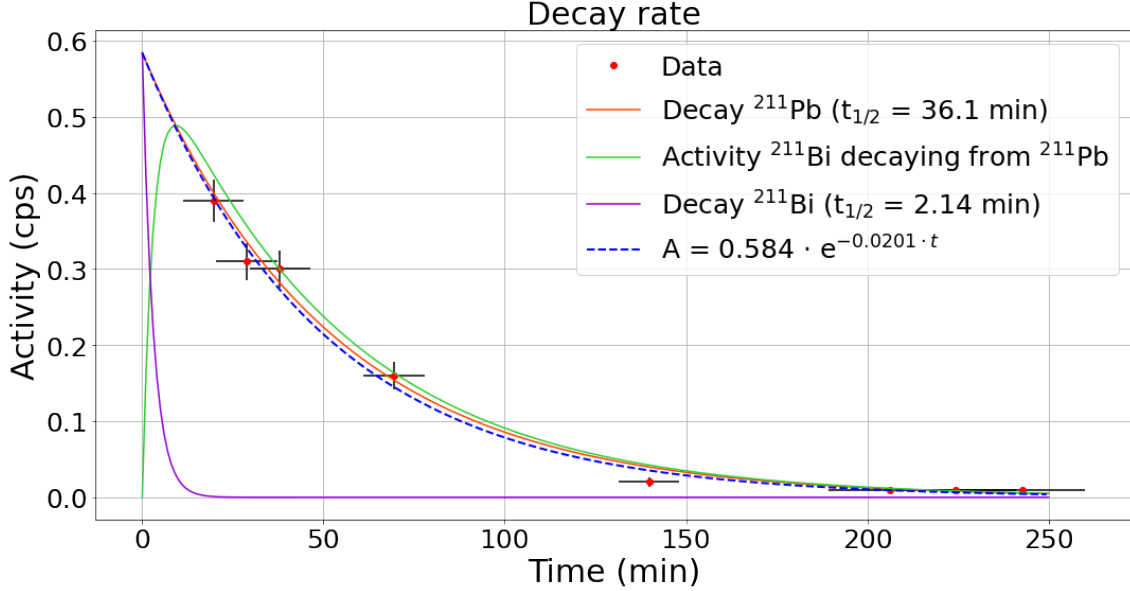

Figure 26: *Decay rate of the Bi I peak shown in Figure 24. The plot shows the data points for the average measured activity after a certain amount of time had passed. The blue dotted line indicates the fit function of the data points, where the fit is indicated in the legend. The purple and orange lines indicate the decay of ^{211}Bi and ^{211}Pb, respectively. The green line indicates the activity of ^{211}Bi decaying from ^{211}Pb. It was assumed that $A_0 = 0.584$ cps was the starting activity of ^{211}Bi and ^{211}Pb.*

Figure 26 also indicates the decays from ^{211}Bi and ^{211}Pb. From the extrapolated fit function, the determined starting activity, $A_0 = 0.584$ cps, is assumed to be the starting activity of ^{211}Bi and ^{211}Pb. The activities of ^{211}Bi and ^{211}Pb are calculated using the radioactive decay law (Equation 11). The activity of ^{211}Bi decaying from ^{211}Pb is dependent on its own decay as well as the rate at which ^{211}Pb decays, forming new ^{211}Bi nuclei. This can be calculated using the following equation:

$$A_2 = \frac{\lambda_2}{\lambda_2 - \lambda_1} A_1^0 \left(e^{-\lambda_1 t} - e^{-\lambda_2 t} \right) + A_2^0 e^{-\lambda_2 t} \tag{15}$$

where the first term in the equation represents the number of ^{211}Bi nuclei formed in the decay of ^{211}Pb, and the second term represents the decay of the ^{211}Bi nuclide. λ_2 and A_2^0 are the decay constant and the initial activity of ^{211}Bi, respectively, λ_1 and A_1^0 are the decay constant and the initial activity of ^{211}Pb, respectively. In Figure 26, the purple and orange lines show the decay of ^{211}Bi and ^{211}Pb, respectively. The green line indicates the activity of ^{211}Bi decaying from ^{211}Pb, which is assumed to be zero at time $t = 0$.

The nuclides reach transient equilibrium after a certain amount of time has passed. This means that parent-daughter nuclides decay at the same half-life, that of the parent nuclide [50]. After ~ 9 min, the ^{211}Bi decaying from ^{211}Pb starts to decay with approximately the same half-life as its parent nuclide, ^{211}Pb. Hence, it is expected to find the half-life of ^{211}Pb from the fit function.

33

The half-life can be calculated according to the following equation:

$$t_{1/2} = \frac{\ln(2)}{\lambda} \tag{16}$$

where λ is the decay constant. From the data in Figure 26, the decay constant is determined to be $\lambda = 0.0201 \pm 0.0015$ per min. Using Equations 16 and 29, the half-life and its uncertainty are calculated to be $t_{1/2} = 34.5 \pm 2.6$ min. This corresponds to the half-life of ^{211}Pb, which confirms that the measured peaks correspond to ^{211}Bi.

4.3   Results

As determined in Section 4.2.3, ^{211}Pb is extracted from the gas catcher and captured on the aluminium mesh. From here, it decays into ^{211}Bi which is identified by the detector. However, this was not the result that was expected. Multiple measurements were performed by changing the voltages of the DC electronics and the RF carpet. A summary of the results is given in Table 7.

Table 7: *Summary of the measurements performed by changing the voltages of the DC electronics and the RF carpet. The DC electronics include the DC cage, DC carpet, and target holder.*

Pressure (mbar)	RF carpet (V_{pp})	DC cage (V)	DC carpet (V)	Target holder (V)	Mesh (V)	^{211}Bi peaks observed
50	off	0	0	0	-3000	yes
50	79, 96	0	0	0	-3000	yes
50	79, 98	0	150	0	-3000	no
50	79, 98	300	150	0	-3000	no
50	79, 98	300	163	0	-3000	no
50	79, 98	300	163	50	-3000	no
50	79, 98	300	120	50	-3000	no
50	79, 98	300	0	50	-3000	yes

When all the electronics were off, ^{211}Bi peaks were observed, and when all the electronics were on, there were no peaks observed. Hence, it was concluded that something in the electronics was not working. Through systematic studies (Table 7), it was found that the DC field of the carpet was blocking the ions. When the DC carpet was on, and there was no voltage applied to the DC cage and the target holder, no ions were extracted. Changing the voltages on the DC cage and target holder, and increasing and decreasing the voltage on the DC carpet, did not result in any peaks. As soon as the voltage on the DC carpet was turned off, the two ^{211}Bi peaks appeared. Hence, it was decided to measure the gradient of the DC carpet and the DC cage to verify if they were working.

In Appendix B, Section B.1, the measured voltages on the ring electrodes of the cage are given in Table 8. Figure 29 show how the rings were numbered. For these measurements a voltage of 300 V was given at the power supply. This value is taken because in the simulations from B. Anđelić [27], a DC gradient of 7 V/cm is used. Also, L. Blaauw [46] performed measurements to determine how many ions were guided to the carpet for different cage voltages up to 300 V. The most ions were guided to the carpet when the voltage on the DC cage was set to 300 V. For a voltage of 300 V at the power supply, the measured voltage on the grid electrode was 299.6 ± 0.1 V and on the last electrode (#16), closest to the RF carpet, a voltage of 0 V was measured. A gradual decrease of ~ 20 V was measured at each ring electrode. This results in a DC gradient of:

$$\frac{(299.6 - 0)}{44.3} \approx 6.8 \, \text{V/cm} \tag{17}$$

The measurement results of Table 8 are also plotted and shown in Figure 28. The data points follow a straight line. Hence, the DC gradient measurement results verify that the electronics of the DC cage work correctly.

The DC gradient of the RF carpet was determined by measuring the voltage on the outer- and inner ring electrodes of the carpet, as shown in Figure 27. One measurement of the voltage on the ring halfway on the carpet was included as well. The DC gradient was calculated for different voltages that were applied at the power supply. For each value, the voltage on the outer- and inner ring electrode was measured. The results are given in Appendix B, Section B.2, Table 9.
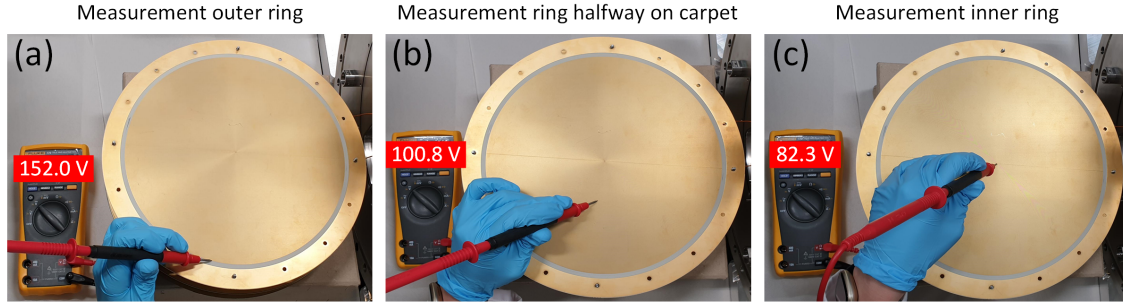

Figure 27: *Measurements of the voltage on the concentric ring electrodes of the RF carpet. (a) Measurement of the voltage on the outer ring electrode. (b) Measurement of the voltage on a ring electrode halfway across the carpet. (c) Measurement of the voltage on the inner ring electrode, the extraction orifice. The measured voltages are indicated in the figures. A voltage of 151 V was given at the power supply.*

In the simulations performed by B. Anđelić [27], a DC gradient of $3\,\mathrm{V/cm}$ was used for the carpet. With the radius of the carpet being equal to $r = 12.5\,\mathrm{cm}$, this results in a voltage of $37.5\,\mathrm{V}$. From the DC gradient measurements given in Appendix B.2, Table 9, a gradient of $1.465\,\mathrm{V/cm}$ was measured for a given voltage of $39\,\mathrm{V}$. This is not even close to the $3\,\mathrm{V/cm}$, which was in disagreement with the design specifications.

In the experiments, the highest possible voltage that could be applied before breakdown, was $151\,\mathrm{V}$. For this, the measured voltage on the outer ring electrode is equal to $152.0 \pm 0.1\,\mathrm{V}$, and on the inner ring electrode it is equal to $82.3 \pm 0.1\,\mathrm{V}$. However, the inner ring electrode is supposed to be equal to $0\,\mathrm{V}$. The voltages were also measured at the back side of the carpet, at the resistors. The results are indicated in the picture of the back side of the carpet, see Figure 30, and are also plotted and shown in Figure 31. It was expected to see a gradual decrease in voltage from the outer ring to the inner ring, following a straight line. However, the results show that the voltage decreases faster for the outer rings compared to the inner rings.

Hence, it is concluded that the DC field of the RF carpet is not working as expected.

5 Discussion

From the experiments, it was concluded that ^{211}Pb, and therefore ^{211}Bi, was extracted from the gas cell. However, it was found that these nuclei were only extracted when the voltage on the DC carpet was turned off. This means that the DC ion guiding of the RF carpet is not working as expected, which leads to longer transportation- and slower extraction times. This might also be the reason why the ^{219}Rn and ^{215}Po nuclei were not extracted. The ^{219}Rn and ^{215}Po ions have half-lives of 3.96 s and 1.78 ms, respectively. If the extraction time is not fast enough, the ^{219}Rn and ^{215}Po decay or recombine in the gas cell, and are lost. Since the half-life of ^{211}Pb is much larger ($t_{1/2} = 36.1$ min), there is more time to extract these ions before they decay. Hence, for future experiments, it is recommended to perform more research into the working of the DC field. Proper ion guiding by electric fields helps reducing the extraction time.

Another reason why the ^{219}Rn ions might not be extracted is the gas purity. Impurities in the gas lead to undesired ion losses. The ^{219}Rn ions can neutralize through collisions with the helium buffer gas or impurities. Usually, to reduce the amount of impurities and enhance the ion survival probability, the gas cell is operated at cryogenic temperatures [9, 15, 36, 41]. However, in the CISe setup, the gas cell is operated at room temperature. It is essential for the gas cell to be operated at ultra-pure conditions: ultra-high vacuum and ultra-high buffer gas purity [16, 41, 51, 52]. Although the gas cell was frequently baked to reduce impurities and reach high-vacuum conditions, the measurements in these thesis were performed with a helium purity of 5.0 (Linde). To reduce the amount of impurities in the helium gas, a cold-trap was used. Measurements to extract ^{219}Rn recoils from a gas catcher operated at room temperature have already been performed with moderate helium gas purity (4.6) and a cold-trap [17]. It was concluded that the highest purity of the helium gas does not necessarily provide the highest efficiency. The ions can only reach the 2^+ charge state when they collide with the helium. Thus, for increased impurity levels, the doubly charged ions will reduce to single charged ions [17], leading to higher efficiencies.

Although it should be possible to extract ions from a gas catcher using a lower buffer gas purity, it is recommended to employ high-purity conditions. Thus, measurements with a helium purity of 6.0. In combination with a cold-trap, this will reduce the level of impurities even further and the influence on the measurement results can be examined.

There were also some limitations specific to the setup. One of them is the "RF carpet box", which was used to give the RF signal to the carpet. A picture of the RF box is shown in Appendix C, Figure 32. It shows that the RF box is a bit tilted because of the connection point of the cable. Because of this, it is possible that the wires inside touch. This is not desired since these wires are not insulated. For the short term this was solved by wrapping Kapton tape around the wires for insulation. However, it was not always possible to produce a stable signal. Hence, for the long term, it is recommended to design a new RF box that runs in a more stable manner.

Another issue which might be worth looking into, is the heat dissipation of the RF carpet. High RF powers create a lot of heat which can damage the electrical components of the carpet. A change in the RF power leads to a change in the RF carpet temperature. The number of detected α-particles are dependent on this temperature [51]. A coil is soldered on the back side of the carpet (Figure 10(c)), which ensures the heat is dissipated. However, at high temperatures, the coil can fall off. If it is not possible to provide the necessary RF voltage without damaging the electrical components, an alternative design may have to be found.

Since the gas catcher was operated at room temperature, there were some problems with performing measurements in summer. When it was very warm outside, the temperature in the lab rose as well. This resulted in unstable conditions where it was sometimes not possible to perform measurements. Although this is not something one can prevent, it is recommended to perform the measurements when the temperatures are more stable around 20 °C.

6 Summary & conclusion

In this thesis, the ion guiding in- and ion extraction from the gas catcher were examined by performing α-spectrometry. A detector holder was designed for this purpose and installed behind the RF carpet. A radioactive ion source, ^{223}Ra, was mounted inside the gas catcher. In the first experiments, different ion capture materials were tested. The measurement with the aluminium mesh had the best performance, and was used in the carpet measurements. The carpet measurements confirmed the ion extraction of ^{211}Bi (Figure 24), but not as expected: a problem in the ion guiding process was found. The ^{211}Pb ions, and therefore the ^{211}Bi ions, were only extracted when the voltage on the DC carpet was off. This resulted in slower extraction times since the DC guiding of the carpet was not working. This might also be the reason why ^{219}Rn ($t_{1/2} = 3.96\,\text{s}$) and ^{215}Po ($t_{1/2} = 1.78\,\text{ms}$) were not detected. This problem has to be solved to decrease the extraction time before continuing with the measurements. Other possible future adjustments include the purity of the helium buffer gas, the stable operation of the RF box, and the heat dissipation of the RF carpet. When a proper ion extraction is achieved, the performance of the setup can be optimized by tuning the RF with the DC electronics. The next step would be moving the radioactive source from target holder #2 to target holder #1 (Figure 11(a)), further away from the carpet, to examine the differences. Another future experiment would be moving the detector further behind the RF carpet, to test the guiding of the ions through the ion guide (Figure 3).

References

[1] M. Wang, G. Audi, F. G. Kondev, W. J. Huang, S. Naimi, and X. Xu. The AME2016 atomic mass evaluation (II). Tables, graphs and references. *Chinese Physics C*, 41(3):030003, March 2017.

[2] H. Schatz, A. Aprahamian, V. Barnard, L. Bildsten, A. Cumming, M. Ouellette, T. Rauscher, F.-K. Thielemann, and M. Wiescher. End Point of the *rp* Process on Accreting Neutron Stars. *Phys. Rev. Lett.*, 86(16):3471–3474, April 2001.

[3] M. Mougeot, D. Atanasov, J. Karthein, R. N. Wolf, P. Ascher, K. Blaum, K. Chrysalidis, G. Hagen, J. D. Holt, W. J. Huang, G. R. Jansen, I. Kulikov, Yu. A. Litvinov, D. Lunney, V. Manea, T. Miyagi, T. Papenbrock, L. Schweikhard, A. Schwenk, T. Steinsberger, S. R. Stroberg, Z. H. Sun, A. Welker, F. Wienholtz, S. G. Wilkins, and K. Zuber. Mass measurements of $^{99-101}$In challenge ab initio nuclear theory of the nuclide ^{100}Sn. *Nature Physics*, 17:1099–1103, September 2021.

[4] A. Martín, D. Ackermann, G. Audi, K. Blaum, M. Block, A. Chaudhuri, Z. Di, S. Eliseev, R. Ferrer, D. Habs, F. Herfurth, F. P. Heßberger, S. Hofmann, H.-J. Kluge, M. Mazzocco, M. Mukherjee, J. B. Neumayr, Yu. Novikov, W. Plaß, S. Rahaman, C. Rauth, D. Rodriguez, C. Scheidenberger, L. Schweikhard, P. G. Thirolf, G. Vorobjev, and C. Weber. Mass measurements of neutron-deficient radionuclides near the end-point of the rp-process with SHIPTRAP. *The European Physical Journal A*, 34:341–348, December 2007.

[5] M. Chartier, G. Auger, W. Mittig, A. Lépine-Szily, L. K. Fifield, J. M. Casandjian, M. Chabert, J. Fermé, A. Gillibert, M. Lewitowicz, M. Mac Cormick, M. H. Moscatello, O. H. Odland, N. A. Orr, G. Politi, C. Spitaels, and A. C. C. Villari. Mass Measurement of ^{100}Sn. *Phys. Rev. Lett.*, 77(12):2400–2403, September 1996.

[6] F. Giacoppo, K. Blaum, M. Block, M. Poudyal Chhetri, Ch. E. Düllmann, C. Droese, S. Eliseev, P. Filianin, S. Götz, Y. Gusev, F. Herfurth, F. P. Hessberger, O. Kaleja, J. Khuyag-baatar, M. Laatiaoui, F. Lautenschläger, C. Lorenz, G. Marx, E. Minaya Ramirez, A. K. Mistry, Yu. N. Novikov, W. R. Plass, S. Raeder, D. Rodríguez, D. Rudolph, L. G. Sarmiento, C. Scheidenberger, L. Schweikhard, P. Thirolf, and A. Yakushev. Recent upgrades of the SHIPTRAP setup: On the finish line towards direct mass spectroscopy of superheavy elements. *Acta Physica Polonica B*, 48(3):423–429, March 2017.

[7] J. B. Neumayr, L. Beck, D. Habs, S. Heinz, J. Szerypo, P. G. Thirolf, V. Varentsov, F. Voit, D. Ackermann, D. Beck, M. Block, Z. Di, S. A. Eliseev, H. Geissel, F. Herfurth, F. P. Heßberger, S. Hofmann, H.-J. Kluge, M. Mukherjee, G. Münzenberg, M. Petrick, W. Quint, S. Rahaman, C. Rauth, D. Rodríguez, C. Scheidenberger, G. Sikler, Z. Wang, C. Weber, W. R. Plaß, M. Breitenfeldt, A. Chaudhuri, G. Marx, L. Schweikhard, A. F. Dodonov, Y. Novikov, and M. Suhonen. The ion-catcher device for SHIPTRAP. *Nuclear Instruments and Methods in Physics Research Section B: Beam Interactions with Materials and Atoms*, 244(2):489–500, March 2006.

[8] M. Ranjan, S. Purushothaman, T. Dickel, H. Geissel, W. R. Plass, D. Schäfer, C. Scheidenberger, J. Van de Walle, H. Weick, and P. Dendooven. New stopping cell capabilities: RF carpet performance at high gas density and cryogenic operation. *EPL (Europhysics Letters)*, 96(5):52001, November 2011.

[9] C. Droese, S. Eliseev, K. Blaum, M. Block, F. Herfurth, M. Laatiaoui, F. Lautenschläger, E. Minaya Ramirez, L. Schweikhard, V. V. Simon, and P. G. Thirolf. The cryogenic gas stopping cell of SHIPTRAP. *Nuclear Instruments and Methods in Physics Research Section B: Beam Interactions with Materials and Atoms*, 338:126–138, November 2014.

[10] A. Mollaebrahimi, B. Anđelić, J. Even, M. Block, M. Eibach, F. Giacoppo, N. Kalantar-Nayestanaki, O. Kaleja, H. R. Kremers, M. Laatiaoui, and S. Raeder. A setup to develop novel Chemical Isobaric SEparation (CISE). *Nuclear Instruments and Methods in Physics*

Research, Section B: Beam Interactions with Materials and Atoms, 463:508–511, January 2020.

[11] A. Shayesteh, V. V. Lavrov, G. K. Koyanagi, and D. K. Bohme. Reactions of Atomic Cations with Methane: Gas Phase Room-Temperature Kinetics and Periodicities in Reactivity. *The Journal of Physical Chemistry A*, 113(19):5602–5611, 2009.

[12] A. Mollaebrahimi. *Mass and half-life measurements of neutron-deficient isotopes with A~100 and developments for the FRS Ion Catcher and CISE*. PhD thesis, University of Groningen, 2021.

[13] J. Ärje, J. Äystö, H. Hyvönen, P. Taskinen, V. Koponen, J. Honkanen, A. Hautojärvi, and K. Vierinen. Submillisecond On-Line Mass Separation of Nonvolatile Radioactive Elements: An Application of Charge Exchange and Thermalization Processes of Primary Recoil Ions in Helium. *Phys. Rev. Lett.*, 54(2):99–101, January 1985.

[14] Y. Kudryavtsev, B. Bruyneel, M. Huyse, J. Gentens, P. Van den Bergh, P. Van Duppen, and L. Vermeeren. A gas cell for thermalizing, storing and transporting radioactive ions and atoms. Part I: Off-line studies with a laser ion source. *Nuclear Instruments and Methods in Physics Research Section B: Beam Interactions with Materials and Atoms*, 179(3):412–435, August 2001.

[15] P. Dendooven, S. Purushothaman, and K. Gloos. On a cryogenic noble gas ion catcher. *Nuclear Instruments and Methods in Physics Research Section A: Accelerators, Spectrometers, Detectors and Associated Equipment*, 558(2):580–583, March 2006.

[16] G. Savard, J. Clark, C. Boudreau, F. Buchinger, J. E. Crawford, H. Geissel, J. P. Greene, S. Gulick, A. Heinz, J. K. P. Lee, A. Levand, M. Maier, G. Münzenberg, C. Scheidenberger, D. Seweryniak, K. S. Sharma, G. Sprouse, J. Vaz, J. C. Wang, B. J. Zabransky, and Z. Zhou. Development and operation of gas catchers to thermalize fusion–evaporation and fragmentation products. *Nuclear Instruments and Methods in Physics Research Section B: Beam Interactions with Materials and Atoms*, 204:582–586, may 2003.

[17] J. Huikari, P. Dendooven, A. Jokinen, A. Nieminen, H. Penttilä, K. Peräjärvi, A. Popov, S. Rinta-Antila, and J. Äystö. Production of neutron deficient rare isotope beams at IGISOL; on-line and off-line studies. *Nuclear Instruments and Methods in Physics Research Section B: Beam Interactions with Materials and Atoms*, 222(3-4):632–652, August 2004.

[18] J. F. Ziegler, M. D. Ziegler, and J. P. Biersack. SRIM – The stopping and range of ions in matter (2010). *Nuclear Instruments and Methods in Physics Research Section B: Beam Interactions with Materials and Atoms*, 268(11-12):1818–1823, June 2010.

[19] D. J. Morrissey, G. Bollen, M. Facina, and S. Schwarz. Pulsed extraction of ionization from helium buffer gas. *Nuclear Instruments and Methods in Physics Research Section B: Beam Interactions with Materials and Atoms*, 266(21):4822–4828, November 2008.

[20] A. Takamine, M. Wada, Y. Ishida, T. Nakamura, K. Okada, Y. Yamazaki, T. Kambara, Y. Kanai, T. M. Kojima, Y. Nakai, N. Oshima, A. Yoshida, T. Kubo, S. Ohtani, K. Noda, I. Katayama, P. Hostain, V. Varentsov, and H. Wollnik. Space-charge effects in the catcher gas cell of a rf ion guide. *Review of Scientific Instruments*, 76(10):103503, 2005.

[21] M. Facina, G. Bollen, and D. J. Morrissey. Space charge effects on stopped projectile fragment drift in gas. *Hyperfine Interactions*, 174:21–26, 2007.

[22] R. Ringle, G. Bollen, K. Lund, C. Nicoloff, S. Schwarz, C. S. Sumithrarachchi, and A. C. C. Villari. Particle-in-cell techniques for the study of space charge effects in the Advanced Cryogenic Gas Stopper. *Nuclear Instruments and Methods in Physics Research Section B: Beam Interactions with Materials and Atoms*, 496:61–70, June 2021.

[23] M. Huyse, M. Facina, Y. Kudryavtsev, P. Van Duppen, and ISOLDE collaboration. Intensity limitations of a gas cell for stopping, storing and guiding of radioactive ions. *Nuclear Instruments and Methods in Physics Research Section B: Beam Interactions with Materials and Atoms*, 187(4):535–547, April 2002.

[24] M. Facina, B. Bruyneel, S. Dean, J. Gentens, M. Huyse, Y. Kudryavtsev, P. Van den Bergh, and P. Van Duppen. A gas cell for thermalizing, storing and transporting radioactive ions and atoms. Part II: On-line studies with a laser ion source. *Nuclear Instruments and Methods in Physics Research Section B: Beam Interactions with Materials and Atoms*, 226(3):401–418, November 2004.

[25] F. Paschen. Ueber die zum Funkenübergang in Luft, Wasserstoff und Kohlensäure bei verschiedenen Drucken erforderliche Potentialdifferenz. *Annalen der Physik*, 273(5):69–96, 1889.

[26] S. N. Anthony, D. L. Shinholt, and M. F. Jarrold. A simple electrospray interface based on a DC ion carpet. *International Journal of Mass Spectrometry*, 371:1–7, October 2014.

[27] B. Anđelić. *Direct mass measurements of No, Lr and Rf isotopes with SHIPTRAP and developments for chemical isobaric separation.* PhD thesis, University of Groningen, 2021.

[28] S. A. Eliseev, M. Block, A. Chaudhuri, Z. Di, D. Habs, F. Herfurth, H.-J. Kluge, J. B. Neumayr, W. R. Plaß, C. Rauth, P. G. Thirolf, G. Vorobjev, and Z. Wang. Extraction efficiency and extraction time of the SHIPTRAP gas-filled stopping cell. *Nuclear Instruments and Methods in Physics Research Section B: Beam Interactions with Materials and Atoms*, 258(2):479–484, May 2007.

[29] P. Dendooven. The development and status of the IGISOL technique. *Nuclear Instruments and Methods in Physics Research Section B: Beam Interactions with Materials and Atoms*, 126(1–4):182–189, April 1997.

[30] L. Weissman, D. J. Morrissey, G. Bollen, D. A. Davies, E. Kwan, P. A. Lofy, P. Schury, S. Schwarz, C. Sumithrarachchi, T. Sun, and R. Ringle. Conversion of 92 MeV/u ^{38}Ca/^{37}K projectile fragments into thermalized ion beams. *Nuclear Instruments and Methods in Physics Research Section A: Accelerators, Spectrometers, Detectors and Associated Equipment*, 540(2):245–258, March 2005.

[31] G. Bollen. "Ion surfing" with radiofrequency carpets. *International Journal of Mass Spectrometry*, 299(2–3):131–138, January 2011.

[32] M. Brodeur, A. E. Gehring, G. Bollen, S. Schwarz, and D. J. Morrissey. Experimental investigation of the ion surfing transport method. *International Journal of Mass Spectrometry*, 336:53–60, February 2013.

[33] F. Arai, Y. Ito, M. Wada, P. Schury, T. Sonoda, and H. Mita. Investigation of the ion surfing transport method with a circular rf carpet. *International Journal of Mass Spectrometry*, 362:56–58, April 2014.

[34] W. X. Huang, P. Dendooven, K. Gloos, N. Takahashi, J. P. Pekola, and J. Äystö. Extraction of radioactive positive ions across the surface of superfluid helium: A new method to produce cold radioactive nuclear beams. *Europhysics Letters (EPL)*, 63(5):687–693, September 2003.

[35] S. Purushothaman, P. Dendooven, I. Moore, H. Penttilä, J. Ronkainen, A. Saastamoinen, J. Äystö, K. Peräjärvi, N. Takahashi, and K. Gloos. Cryogenic helium as stopping medium for high-energy ions. *Nuclear Instruments and Methods in Physics Research Section B: Beam Interactions with Materials and Atoms*, 266(19-20):4488–4492, October 2008.

[36] W. R. Plaß, T. Dickel, S. Purushothaman, P. Dendooven, H. Geissel, J. Ebert, E. Haettner, C. Jesch, M. Ranjan, M. P. Reiter, H. Weick, F. Amjad, S. Ayet, M. Diwisch, A. Estrade, F. Farinon, F. Greiner, N. Kalantar-Nayestanaki, R. Knöbel, J. Kurcewicz, J. Lang, I. Moore, I. Mukha, C. Nociforo, M. Petrick, M. Pfützner, S. Pietri, A. Prochazka, A.-K. Rink, S. Rinta-Antila, D. Schäfer, C. Scheidenberger, M. Takechi, Y. K. Tanaka, J. S. Winfield, and M. I.

Yavor. The FRS Ion Catcher – A facility for high-precision experiments with stopped projectile and fission fragments. *Nuclear Instruments and Methods in Physics Research Section B: Beam Interactions with Materials and Atoms*, 317:457–462, December 2013.

[37] I. Miskun, T. Dickel, I. Mardor, C. Hornung, D. Amanbayev, S. A. San Andrés, J. Bergmann, J. Ebert, H. Geissel, M. Górska, F. Greiner, E. Haettner, W. R. Plaß, S. Purushothaman, C. Scheidenberger, A.-K. Rink, H. Weick, S. Bagchi, P. Constantin, S. Kaur, W. Lippert, B. Mei, I. Moore, J.-H. Otto, S. Pietri, I. Pohjalainen, A. Prochazka, C. Rappold, M. P. Reiter, Y. K. Tanaka, J. S. Winfield, and For the Super-FRS Experiment Collaboration. A novel method for the measurement of half-lives and decay branching ratios of exotic nuclei. *The European Physical Journal A*, 55(9), September 2019.

[38] N. Vajda, P. Martin, and C.-K. Kim. Chapter 6 - Alpha Spectrometry. In M. F. L'Annunziata, editor, *Handbook of Radioactivity Analysis (Third Edition)*, pages 363–422. Academic Press, third edition edition, 2012.

[39] G. Choppin, J.-O. Liljenzin, and J. Rydberg. CHAPTER 8 - Detection and Measurement Techniques. In *Radiochemistry and Nuclear Chemistry (Third Edition)*, pages 192–238. Butterworth-Heinemann, 2002.

[40] ORTEC. *Introduction to Charged-Particle Detectors.* Accessed: 2022-08-22. [Online]. Available: `https://www.ortec-online.com/-/media/ametekortec/other/introduction-charged-particle-detectors.pdf?la=en`.

[41] S. Purushothaman. *Superfluid Helium and Cryogenic Noble Gases as Stopping Media for Ion Catchers.* PhD thesis, University of Groningen, 2008.

[42] Y. A. Akovali. Nucl. Data Sheets 72, 191, 1994.

[43] E. Browne. Nucl. Data Sheets 65, 669, 1992.

[44] Chapter 2 - Preamplifiers. In *ORTEC Modular Pulse-Processing Electronics Catalog*, pages 2.1–2.6. Oak Ridge, USA, 2001. Accessed: 2022-08-22. [Online]. Available: `https://www3.nd.edu/~wzech/catalog.pdf`.

[45] Chapter 3 - Amplifiers. In *ORTEC Modular Pulse-Processing Electronics Catalog*, pages 3.1–3.19. Oak Ridge, USA, 2001. Accessed: 2022-08-22. [Online]. Available: `https://www3.nd.edu/~wzech/catalog.pdf`.

[46] L. Blaauw. Production and transmission of ions in the CISe setup. Master's thesis, University of Groningen, October 2021.

[47] Y. Ménesguen and M.-C. Lépy. COLEGRAM, a flexible user-friendly software for processing of ionizing radiation spectra. *Nuclear Instruments and Methods in Physics Research Section A: Accelerators, Spectrometers, Detectors and Associated Equipment*, 1003:165341, July 2021.

[48] Y. Ménesguen. Note Technique LNHB 2020/15, COLEGRAM : Software Presentation and User Manual. Technical report, CEA\LNHB, June 2020.

[49] C. Yalçin. Thickness measurement using alpha spectroscopy and SRIM. *Journal of Physics: Conference Series*, 590:012050, April 2015.

[50] M. F. L'Annunziata. Chapter 1 - Radiation Physics and Radionuclide Decay. In *Handbook of Radioactivity Analysis (Third Edition)*, pages 1–162. Academic Press, 2012.

[51] M. Ranjan. *Design and characterization of a cryogenic stopping cell for radioactive ions.* PhD thesis, University of Groningen, 2012.

[52] M. Maier, C. Boudreau, F. Buchinger, J.A. Clark, J.E. Crawford, J. Dilling, H. Fukutani, S. Gulick, J.K.P. Lee, R.B. Moore, G. Savard, J. Schwartz, and K.S. Sharma. Stopping, Trapping and Cooling of Radioactive Fission Fragments in an Ion Catcher Device. In *Hyperfine Interactions*, volume 132, pages 521–525, January 2001.

[53] D. A. Gedcke. ORTEC Application Note AN59. *How Counting Statistics Controls Detection Limits and Peak Precision*, 2001.

A Error propagation

A.1 Standard deviation of the activity

The standard deviation of the activity is given by:

$$\sigma_c = \frac{\sigma}{t} \tag{18}$$

where σ is the standard deviation, and t the time. Radioactive decay for long-lived isotopes follows the Poisson distribution [53], which means σ is equal to $\sqrt{N}$. N is the total number of counts and is equal to the count rate C times the measurement time t. So equation 18 can be written as:

$$\sigma_c = \frac{\sqrt{N}}{t} \tag{19}$$

$$= \frac{\sqrt{C \cdot t}}{t} \tag{20}$$

$$= \sqrt{\frac{C}{t}} \tag{21}$$

where the count rate C is equal to the activity.

A.2 Uncertainty of the half-life $t_{1/2}$

The half-life is dependent on the measured activity, as shown in Equation 13. The uncertainty in the measured activity propagates to the half-life because of this dependence. The error in the half-life is calculated as follows:

$$\Delta t_{1/2} = \ln(2) \cdot t \cdot \sqrt{\left(\frac{\partial}{\partial A}\left(-\frac{\sigma_A}{\ln\left(\frac{A}{A_0}\right)}\right)\right)^2 + \left(\frac{\partial}{\partial A_0}\left(-\frac{\sigma_{A_0}}{\ln\left(\frac{A}{A_0}\right)}\right)\right)^2} \tag{22}$$

$$= \ln(2) \cdot t \cdot \sqrt{\left(\frac{\sigma_A}{A\ln^2\left(\frac{A}{A_0}\right)}\right)^2 + \left(\frac{\sigma_{A_0}}{A_0\ln^2\left(\frac{A}{A_0}\right)}\right)^2} \tag{23}$$

$$= \ln(2) \cdot t \cdot \sqrt{\frac{\sigma_A^2}{A^2\ln^4\left(\frac{A}{A_0}\right)} + \frac{\sigma_{A_0}^2}{A_0^2\ln^4\left(\frac{A}{A_0}\right)}} \tag{24}$$

$$= \ln(2) \cdot t \cdot \sqrt{\frac{A_0^2\sigma_A^2 + A^2\sigma_{A_0}^2}{A^2 A_0^2 \ln^4\left(\frac{A}{A_0}\right)}} \tag{25}$$

where t is the time between measurements, A is the activity, σ_A is the standard deviation of activity A, A_0 is the activity of the previous measurement, and σ_{A_0} is the standard deviation of activity A_0.

When the values for λ and $\Delta\lambda$ are known, the uncertainty in the half-life can be calculated as follows:

$$\Delta t_{1/2} = \sqrt{\left(\frac{\partial t_{1/2}}{\partial \lambda}\Delta\lambda\right)^2} \tag{26}$$

$$= \sqrt{\left(\frac{\partial\left(\frac{ln(2)}{\lambda}\right)}{\partial\lambda}\Delta\lambda\right)^2} \tag{27}$$

$$= \sqrt{\left(-\frac{\ln(2)}{\lambda^2}\Delta\lambda\right)^2} \tag{28}$$

43

$$= \ln(2) \cdot \frac{\Delta \lambda}{\lambda^2} \tag{29}$$

B DC gradient measurements

B.1 DC cage

The DC gradient of the DC cage was determined by measuring the voltage on the ring electrodes. For these measurements, a voltage of $300\,\text{V}$ was given at the power supply. The results of the measured voltages on each ring are given in Table 8, and are plotted in Figure 28. Figure 29 shows how the rings were numbered. The cage has a length of $443\,\text{mm}$. With this, the DC gradient is calculated to be:

$$\frac{(299.6 - 0)}{44.3} \approx 6.8\,\text{V/cm}$$

Table 8: *DC gradient measurement results for the cage. The voltage given at the power supply is* $300\,\text{V}$.

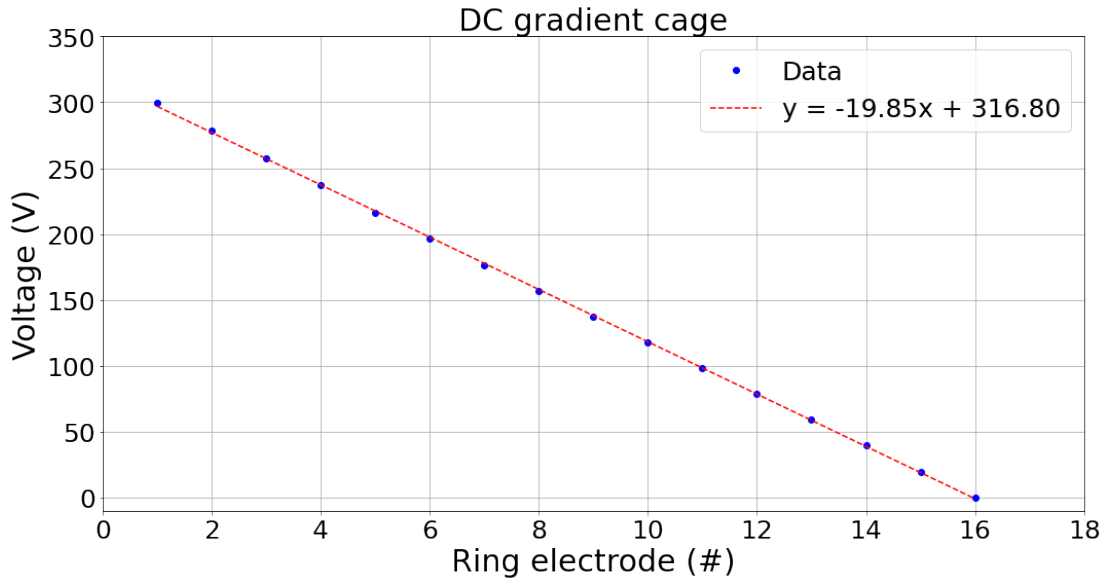| Ring electrode (#)	Voltage (V)
Grid	299.6 ± 0.1
2	278.3 ± 0.1
3	257.4 ± 0.1
4	236.8 ± 0.1
5	216.5 ± 0.1
6	196.4 ± 0.1
7	176.6 ± 0.1
8	156.8 ± 0.1
9	137.2 ± 0.1
10	117.7 ± 0.1
11	98.2 ± 0.1
12	78.7 ± 0.1
13	59.20 ± 0.01
14	39.60 ± 0.01
15	19.88 ± 0.01
16	0

Figure 28: *DC gradient measurement results for the cage, where a voltage of* $300\,\text{V}$ *was applied to the power supply. The uncertainty in the measured values (indicated in Table 8) is smaller than the size of the date points.*

Figure 29: *DC cage structure. The left ring electrode corresponds to the grid electrode or ring electrode #1. The right ring electrode corresponds to #16. In between, ring electrodes #2–#15. The ion stream is also indicated.*

B.2 DC carpet

The DC gradient of the RF carpet was determined by measuring the voltage on the outer- and inner ring electrodes of the carpet. The gradients were determined for different voltages that were applied to the power supply. The results are shown in Table 9. The RF carpet has a diameter of 250 mm.

Table 9: *DC gradient of the RF carpet for different voltages applied at the power supply. The RF carpet has a diameter of 250 mm.*

Voltage at power supply (V)	Voltage outer ring (V)	Voltage inner ring (V)	DC gradient (V/cm)
11	12.40 ± 0.01	6.75 ± 0.01	0.452
24	25.50 ± 0.01	13.86 ± 0.01	0.931
39	40.10 ± 0.01	21.79 ± 0.01	1.465
50	51.01 ± 0.01	27.72 ± 0.01	1.863
74	75.7 ± 0.1	41.14 ± 0.01	2.765
99	100.4 ± 0.1	54.4 ± 0.1	3.68
124	124.9 ± 0.1	67.6 ± 0.1	4.584
148	150.0 ± 0.1	81.2 ± 0.1	5.504
151	152.0 ± 0.1	82.3 ± 0.1	5.576

The voltages were also measured at the back side of the carpet, where the electronic components are situated. The results are shown in Figure 30. A voltage of 151 V was applied to the power supply.
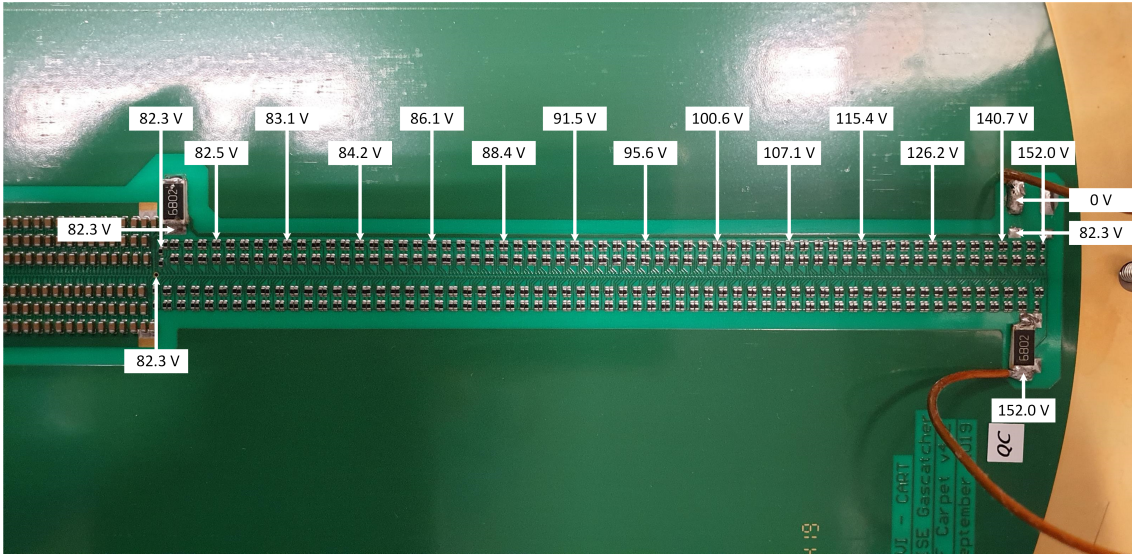
46

Figure 30: *Back side of the RF carpet. The voltage was measured at different resistors indicated in the picture. The uncertainty in the measured values is* 0.1 V.
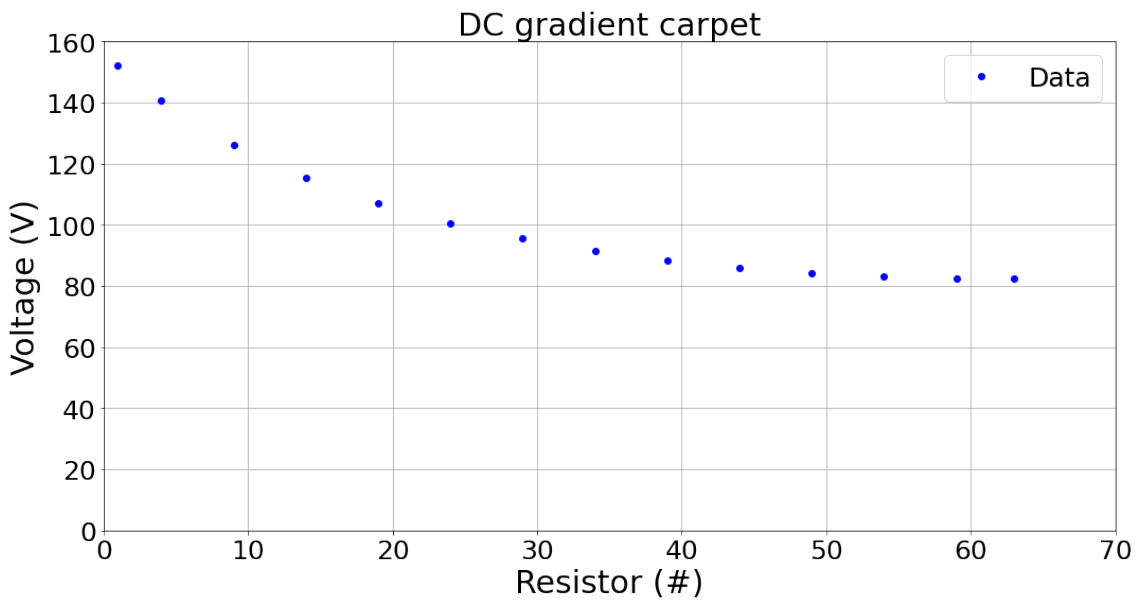

Figure 31: *DC gradient measurement results for the RF carpet, where a voltage of* 151 V *was applied to the power supply. The voltage was measured at different resistors, as indicated in the Figure 30. The uncertainty in the measured values is* 0.1 V, *which is smaller than the size of the data points.*

47

C   RF carpet box

Figure 32: *Picture of the RF carpet box.*